PERGAMON

International Journal of Solids and Structures 38 (2001) 3039–3071

INTERNATIONAL JOURNAL OF SOLIDS and STRUCTURES

www.elsevier.com/locate/ijsolstr

Delamination buckling and growth for delaminations at different depths in a slender composite panel

K.-F. Nilsson [a,*], L.E. Asp [a,b,1], J.E. Alpman [a,c], L. Nystedt [a,d,2]

[a] *The Aeronautical Research Institute of Sweden, Box 110 21, SE-161 11 Bromma, Sweden*
[b] *Swedish Institute for Composites, Box 104, 431 22 Mölndal, Sweden*
[c] *Cap Gemini Sweden, Gustavslundsvägen 131, Box 825, 161 24 Bromma, Sweden*
[d] *Allgon Systems AB, 187 80 Täby, Sweden*

Received 8 October 1999; in revised form 13 April 2000

Abstract

A numerical and experimental investigation for delamination buckling and growth for slender composite panels loaded in compression is presented. The investigated panels consisted of 35 plies in a cross-ply layup with artificially embedded delaminations inserted after three, five or seven plies from the upper surface. The tests clearly and consistently showed that for all delamination depths, delaminated panels failed by delamination growth slightly below the global buckling load of the undamaged panel, whereas the undelaminated panels failed in compression at global buckling. The analysis was done with a finite element based computational model that accounts for contact between delaminated members and fracture mode separation and where crack propagation was simulated with a moving mesh scheme. For all delamination depths, the analysis showed a dramatic increase in the energy release rate when global buckling takes place. Features seen in the tests were captured in the computational analysis. Excellent agreement with tests was found for loads at which delaminated members buckle, the load for onset of delamination growth and the evolution of delamination, e.g., delamination shape and out-of-plane displacements.

Keywords: Delamination; Buckling; Composites; Fractography; Moving mesh; Fracture mode separation

1. Introduction

Carbon fibre/epoxy composites are increasingly used in aircraft structures due to superior specific strength and stiffness. Impact loading from dropped tools, runway debris, etc., may cause so-called ''barely visible damage''. Delaminations could also appear during manufacturing due to nonperfect processes. Such

* Corresponding author. Address: Institute for Advanced Materials, European Commission, P.O. Box 2, 1755 ZG Petten, Netherlands. Tel.: +31-224-565-656; fax: +31-224-561-568.

E-mail addresses: nilsson@jrc.nl (K.-F. Nilsson), leif.asp@sicomp.se (L.E. Asp), johan.alpman@capgemini.se (J.E. Alpman), lennart.nystedt@allgon.se (L. Nystedt).

[1] Tel.: +46-31-706-63-49; fax: +46-31-706-63-63.

[2] Tel.: +46-8-540-834-09; fax: +46-540-824-85.

0020-7683/01/$ - see front matter
PII: S0020-7683(00)00189-X

damage is a serious problem since it may severely reduce the integrity of the structure without being detected. Impact damage usually contains multiple delaminations, which significantly reduce flexural properties of the laminated skin, as well as fractured fibres and matrix cracks. Under compressive loads, interlaminar delaminations often turn out to be the most critical type of damage (Abrate 1991, 1994; Pavier and Clarke, 1996).

When the structure is loaded in compression, delaminations may first buckle and then propagate. Because delaminations often remain undetected, their presence must be considered already in the design phase. Aircraft structures should therefore be designed such that delaminations will arrest prior to a significant reduction of structural properties. Hence, in order to further improve the design, a better understanding of the delamination phenomenon is necessary.

Analysis of delamination buckling and growth is very complex and requires a nonlinear structural analysis in combination with fracture analysis. The material is anisotropic and inhomogeneous and delaminated members tend to be partly in contact. The materials are, however, usually sufficiently brittle to motivate a linear elastic fracture mechanics approach. The fracture toughness for layered materials is usually strongly dependent on the mode mixity, which calls for a decomposition of the crack tip loading into its basic modes. Given the complexity, the way forward has been to start with the simplest cases and gradually increase the complexity of the mathematical model. The development has been described in a large number of papers in the last two decades. A basic understanding of the delamination buckling problem was established in the pioneering works by Chai et al. (1981) and Whitcomb (1981) where one-dimensional "through-width" delaminations were investigated. Elliptical delaminations loaded in uniaxial compression were studied by Chai and Babcock (1985) and in a series of publications by Whitcomb (1989, 1992). The importance of fracture mode separation was demonstrated already in the earliest work of Whitcomb (1981). In all these works, delaminations were always considered to be of particular and a priori known shapes. Delaminations in real structures can have very general shapes. A more general procedure to analyse delamination buckling and growth was presented in a series of papers (Nilsson and Storåkers, 1992; Nilsson, 1993; Nilsson et al., 1993; Giannakopoulos et al., 1994; Nilsson and Giannakopoulos, 1995), where delamination buckling and growth were analysed for quite general delamination fronts, and where contact and mode decomposition were accounted for. Excellent agreement between predictions and test for carbon fibre composites were found for the load required to sustain growth and for the shape of the front during growth (Nilsson et al., 1993).

In all the investigations mentioned above, except the work by Chai et al. (1981), the delaminated member was assumed to be very close to the surface and hence the so-called thin-film assumption could be adopted (i.e., only the delaminated member can have out-of-plane deflection). Aircraft structures are slender. Bending of the substrate and global buckling of the structure may therefore occur prior to delamination growth, which requires that nonlinear kinematics is modelled for the entire structure. It was shown already in the work by Chai et al. (1981) that global bending may increase the energy release rate significantly. A number of papers have since been published on the subject, but often restricted to buckling and post-buckling analyses without delamination growth (Simitses et al., 1985; Kardomateas, 1989; Kim, 1996; Yeh and Tan, 1994). In a recent study of a through-the-width delaminated beam-plate, Sheinman et al. (1998) showed how the energy release rate was affected by the relative dimensions of the delaminated member and the entire structure. In particular a drastic increase in energy release rate was demonstrated when the load approaches the global buckling load.

Basic insight can be gained from the analysis of the through-width delaminations. However, embedded delaminations better represent real-life situations and are also often better suited for experimental studies. In this paper, we present a combined numerical/experimental study for rectangular panels with delaminations inserted at three different depths. The primary objective is to study the interaction between buckling of the delaminated member and global panel buckling. The computational model for general delamination shapes mentioned above was therefore extended to include the effect of global bending.

The outline of this paper is organized as follows: A brief description of the theoretical model and its implementation is first described. This is followed by a detailed discussion of the specimen design, test procedures and test results. Finally, computed results are compared with test results and conclusions are drawn.

2. Theoretical model

2.1. Kinematical and constitutive assumptions

The structure to be analysed consists of a plate of thickness, $t+T$, with a single embedded in-plane delamination with a smooth but otherwise arbitrary front, Γ_D, that encloses an area Ω_D at depth t. The thickness of the delaminated member and the total thickness of the structure are assumed small compared to in-plane dimensions.

The structure is modelled by two plates in the thickness direction with mid-surfaces at $x_3 = t/2$ and $x_3 = -T/2$, respectively, as shown in the one-dimensional illustration in Fig. 1. The displacement of the upper and lower plates are governed by the Reissner–Mindlin assumption, viz,

$$\begin{cases} u_\alpha(x_1,x_2,z) = \overline{u}_\alpha(x_1,x_2) + z\theta_\alpha(x_1,x_2), \\ u_3(x_1,x_2,z) = \overline{u}_3(x_1,x_2). \end{cases} \tag{1}$$

Subscript 1 and 2 refer to in-plane quantities, 3 is the direction normal to the mid-surface, and z is the distance from the mid-surface. Greek indices run from 1 to 2 and θ_α denotes the rotation of a transverse material fibre. An overbar refers to the mid-plane value of the function.

Strains are assumed small and rotations moderate. The small strain tensor may then be written as

$$\begin{cases} e_{\alpha\beta} = e^0_{\alpha\beta} + z\cdot\kappa_{\alpha\beta}, \\ e_{3\alpha} = (\overline{u}_{3,\alpha} + \theta_\alpha)/2, \end{cases} \tag{2}$$

where $e^0_{\alpha\beta} = (\overline{u}_{\alpha,\beta} + \overline{u}_{\beta,\alpha} + \overline{u}_{3,\alpha}\overline{u}_{3,\beta})/2$ is the membrane strain and $\kappa_{\alpha\beta} = (\theta_{\alpha,\beta} + \theta_{\beta,\alpha})/2$, the curvature. The generalized forces conjugate to these quantities can be defined for elastic plates by,

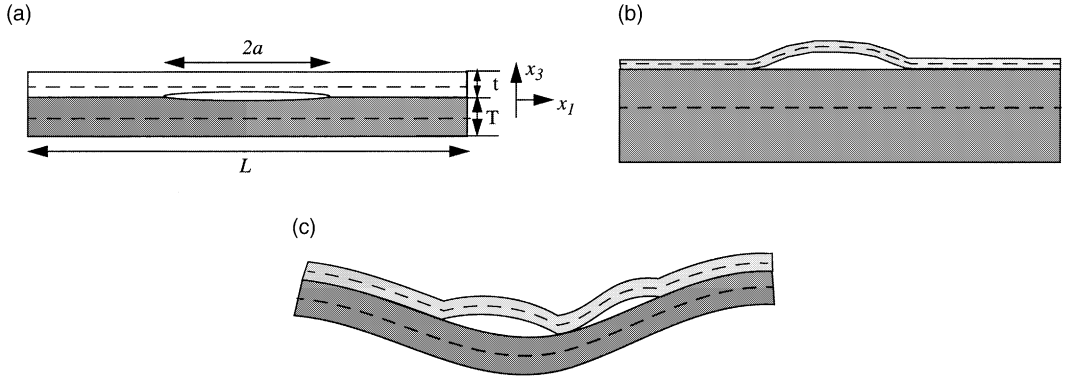

Fig. 1. One-dimensional illustration of a structure with a delamination: (a) undeformed structure, (b) deformed structure when thin film assumption is adopted, and (c) deformed structure which bends globally.

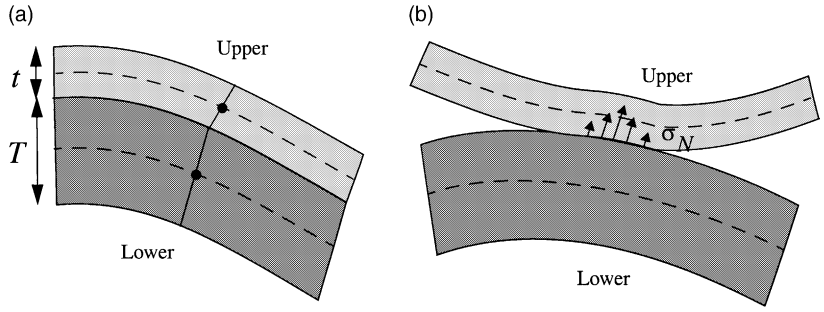

Fig. 2. One-dimensional illustrations of the structural model for (a) undelaminated domain and (b) delaminated domain with contact.

$$N_{\alpha\beta} = \frac{\partial W}{\partial e^0_{\alpha\beta}}, \quad M_{\alpha\beta} = \frac{\partial W}{\partial \kappa_{\alpha\beta}}, \quad 2Q_\alpha = \frac{\partial W}{\partial e_{3\alpha}}, \tag{3}$$

where $W(e^0_{\alpha\beta}, \kappa_{\alpha\beta}, e_{3\alpha})$ denotes the strain energy function.

In the undelaminated domain, displacement continuity is prescribed along the 'interface' as shown in Fig. 2a, which results in three constraint equations linking the upper and lower plate:

$$\begin{cases} \overline{u}^{(\mathrm{U})}_\alpha - \frac{t}{2}\theta^{(\mathrm{U})}_\alpha = \overline{u}^{(\mathrm{L})}_\alpha + \frac{T}{2}\theta^{(\mathrm{L})}_\alpha, \\ \overline{u}^{(\mathrm{U})}_3 = \overline{u}^{(\mathrm{L})}_3, \end{cases} \tag{4}$$

where U and L denote 'upper' and 'lower'. Due to the constraint equations one may consider the stacked plates as a ''two-layer plate model'' with seven degrees of freedom for each node in the x_1x_2 plane.

In most delamination studies based on plate or beam theory (Chai et al., 1981; Sheinman et al., 1998), only one plate is used to describe the deformation in the thickness direction. This is equivalent of also prescribing $\theta^{(\mathrm{L})}_\alpha = \theta^{(\mathrm{U})}_\alpha$ in Eq. (4). This gives a higher transverse shear stiffness than the present model. In a study of the DCB test by Nilsson (1993), the two models were compared with three-dimensional results. The present two-plate model corresponded better to the three-dimensional results for the specific cases studied. The difference was most pronounced at the vertex (i.e., where the delamination front meets a free edge), where the one-plate model gave an artificial peak for the energy release rate which was not seen in the three-dimensional model and the two-plate model. The difference was generally also larger for composite materials than for isotropic materials due to their lower shear stiffness.

In the thin film assumption, $\overline{u}_3 = 0$ and $\theta_\alpha = 0$ are imposed in the undelaminated part as well as for the thicker delaminated member. In that case, the single- and double-plate models are identical.

In the delaminated domain, delaminated members are free to deflect from each other but not to penetrate. This leads to a unilateral contact condition, which may be modelled by the following relation:

$$\begin{cases} \sigma_N(x_1, x_2) = S\frac{2\Delta u_3(x_1,x_2)}{T+t} & \Delta u_3 < 0, \\ \sigma_N(x_1, x_2) = 0 & \Delta u_3 \geqslant 0, \end{cases} \tag{5}$$

where $\sigma_N(<0)$ denotes the resulting contact pressure and Δu_3 the relative transverse deflection between the mid-surface of the upper and lower plate, and S is a measure of transverse stiffness. The unilateral constraint (5) introduces an additional nonlinearity to the structural problem. The a priori unknown contact region as well as the contact forces for a given load are computed by an iterative procedure, which will be outlined in the numerical procedure section below.

2.2. Computation of energy release rate and fracture mode decomposition

Delamination growth is assumed to take place when the energy release rate attains a critical value. For interface crack propagation, the critical energy release rate is usually a function of the basic fracture modes. This is often expressed as $G = G_c(\psi)$, where ψ is the phase angle defined by $\psi = \text{atan}(K_{II}/K_I)$, where K_I and K_{II} are the stress intensity factors in mode I and II (see for instance Hutchinson and Suo (1992)). Thus, analysis of delamination growth requires that the energy release rate as well as the phase angle are computed. Mode mixity formulas usually neglect the mode III effect. For embedded delaminations, this is not a serious problem since the mode III component is usually very small.

The energy release rate at local crack growth, G, can, in the present plate theory, be computed from the discontinuity in field variables across the crack front of a tensor component, P_{nn},

$$G = (P_{nn}^{(1)} - P_{nn}^{(2)}) + (P_{nn}^{(3)} - P_{nn}^{(4)}). \tag{6}$$

Superscript denotes the location where the tensor, P_{nn}, is evaluated (Fig. 3a) where,

$$P_{nn}^{(h)} = W^{(h)} - N_{n\gamma}^{(h)}\overline{u}_{\gamma,n}^{(h)} - Q_n^{(h)}\overline{u}_{3,n}^{(h)} - M_{n\gamma}^{(h)}\theta_{\gamma,n}^{(h)}, \quad h = 1,2,3,4, \tag{7}$$

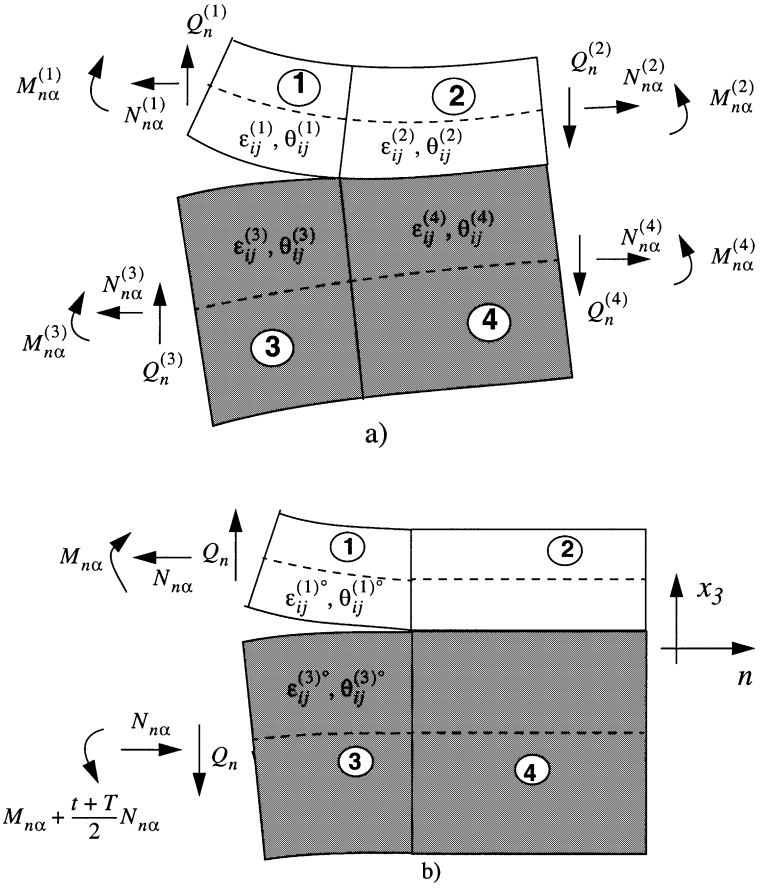

Fig. 3. Split element with resulting beam sectional forces: (a) prior to superposition and (b) after superposition.

and n denotes the normal direction to the crack front. These expressions for the energy release rate were first expressed by Storåkers and Andersson (1988) for von Karman's nonlinear plate theory and the straightforward extension to the Mindlin theory is given in Nilsson et al. (1993).

The nonlinear plate problem may locally be approximated by a linear beam problem by superposing a homogeneous strain field such that the undelaminated region becomes undeformed as shown in Fig. 3b,

$$\begin{cases} \begin{cases} \varepsilon_{ij}^{(h)^\circ} = \varepsilon_{ij}^{(h)} - \varepsilon_{ij}^{(h+1)} \\ \theta_{ij}^{(h)^\circ} = \theta_{ij}^{(h)} - \theta_{ij}^{(h+1)} \end{cases}, & h = 1 \text{ and } 3, \\ \theta_{ij}^{(h)^\circ} = \varepsilon_{ij}^{(h)^\circ} \equiv 0, & h = 2 \text{ and } 4, \end{cases} \tag{8}$$

where superscript h denotes the plate section numbering shown in Fig. 3. Eq. (7) can then be written as

$$P_{nn}^{(h)} = \frac{N_{nn}^{(h)^\circ}\varepsilon_{nn}^{(h)^\circ} + N_{nt}^{(h)^\circ}\varepsilon_{nt}^{(h)^\circ}}{2} + \frac{M_{nn}^{(h)^\circ}\kappa_{nn}^{(h)^\circ}}{2} + \frac{Q_n^{(h)^\circ}\varepsilon_{3n}^{(h)^\circ}}{2}, \tag{9}$$

where superscript o for generalized forces denotes that they are conjugate to the deformation field after superposition. By the virtue of superposition and equilibrium, the number of unknown load resultants for the split beam is reduced to five, which we may denote, $N_{n\alpha}$, $M_{n\alpha}$ and Q_n. The superposition principle was suggested already by Whitcomb (1986) as well as by Suo and Hutchinson (1990). In their analyses, the undelaminated section was modelled as one plate and there was no contribution from the transverse shear forces to the energy release rate as the Kirchhoff assumption was adopted. The fundamental fracture modes as a function of the load resultants can be written as,

$$\begin{cases} K_{\mathrm{I}} = a_1 N_{nn} + a_2 M_{nn} + a_3 Q_n + a_4 N_{nt} + a_5 M_{nt}, \\ K_{\mathrm{II}} = b_1 N_{nn} + b_2 M_{nn} + b_3 Q_n + b_4 N_{nt} + b_5 M_{nt}, \\ K_{\mathrm{III}} = c_1 N_{nn} + c_2 M_{nn} + c_3 Q_n + c_4 N_{nt} + c_5 M_{nt}. \end{cases} \tag{10}$$

The coefficients in Eq. (10) may be determined by solving the split beam problem with sectional forces one by one. This approach was adopted in Nilsson and Storåkers (1992) for the case of isotropic materials using closed form results for the split beam problem given by Hutchinson and Suo (1992) and neglecting the transverse shear contribution. The only nonvanishing coefficients are then

$$\begin{cases} a_1 = \frac{\cos(\omega)}{\sqrt{2tU}}, & a_2 = \frac{\sin(\omega+\gamma)}{\sqrt{2t^3V}}, \\ b_1 = \frac{\sin(\omega)}{\sqrt{2tU}}, & b_2 = \frac{\cos(\omega+\gamma)}{\sqrt{2t^3V}}, \\ c_4 = \sqrt{\frac{t+T}{2tT}}, & \end{cases} \tag{11}$$

and where $\eta = t/(T+t)$ is the thickness ratio, and γ, ω, V and U geometry functions.

$$\begin{cases} 1/V = 12(1+3\eta^3), & 1/U = 1 + 4\eta + 6\eta^2 + 3\eta^3, \\ \gamma = \operatorname{asin}(\sqrt{UV}6\eta^2(1+\eta)), & \omega = 52.1^\circ - 3^\circ\eta. \end{cases} \tag{12}$$

Mode decomposition coefficients for orthotropic bi-materials and when principal material axes are normal to the crack front (corresponding to Eqs. (11) and (12)) are given by Suo and Hutchinson (1990), Hutchinson and Suo (1992) and by Sheinman and Kardomateas (1997).

The crack tip loading depends on constitutive properties, layup sequence, geometry and loading. In general, fibres are not normal to the front and all three fracture modes will be coupled. The split beam problem in such cases has to be solved numerically under generalized plain strain for the particular material combination.

Procedures for reliable calculation of stress intensity factors along edges in piecewise homogeneous and orthotropic materials have been implemented in the in-house FE-solver STRIPE. First, an *hp* version of the finite element method is used to calculate the displacements, u_i. Secondly, a so-called advanced extraction

procedure is used to extract complex-valued stress intensity functions, $C_{k,l}$, in the expression (Andersson et al., 1990; Andersson, 1993),

$$\left\{ \begin{pmatrix} u_n(x_l,x_t,x_3) \\ u_t(x_l,x_t,x_3) \\ u_3(x_l,x_t,x_3) \end{pmatrix} = \sum_{l=1}^{3}\sum_{k=1}^{6} C_{k,l}(x_t)[Z_k(x_l,x_3)]^{\lambda^{(l)}} \begin{pmatrix} \Phi_1^{(k,l)}(x_l,x_3) \\ \Phi_2^{(k,l)}(x_l,x_3) \\ \Phi_3^{(k,l)}(x_l,x_3) \end{pmatrix}, \right. \tag{13}$$

which uniquely characterizes the displacements near the delamination front. In Eq. (13), $Z_k(x_l,x_3)$ and $\Phi(x_l,x_3)$ are complex functions derived according to the theory of Lekhnitskii (1963) and $\lambda^{(l)}\, l = 1$, 2 and 3 the complex singularity exponents. For the crack problem, $\lambda^{(1)} = 0.5$, $\lambda^{(2)} = 0.5 + i\varepsilon$, and $\lambda^{(3)} = 0.5 - i\varepsilon$. In most practical examples, $\varepsilon \ll 1$ and when the material properties are identical on either side of the delamination interface, ε is identically zero.

When $\varepsilon \neq 0$, the mathematical solution gives a (usually very) small region with oscillatory stresses and associated interpenetration with increasing frequency as the crack tip is approached. Consequently, classical stress intensity factors cannot be defined (i.e., $K_{\mathrm{I}} = \lim_{x_n\to 0}\sigma_{33}\sqrt{2\pi x_n}$, $K_{\mathrm{II}} = \lim_{x_n\to 0}\tau_{n3}\sqrt{2\pi x_n}$), and in particular the mode ratio is not defined. This problem is discussed in the comprehensive papers by Rice (1988) and Hutchinson and Suo (1992). One drastic way to circumvent this problem is to simply prescribe $\varepsilon = 0$, and the classical stress intensity factors can be retrieved. In the STRIPE code, stress intensities defined by,

$$\left\{ \begin{aligned} K_1(x_t) &= \lim_{x_n\to 0}\sum_{l=1}^{3}\sum_{k=1}^{6}(\sqrt{2\pi})x_l^{(1-\lambda^{(l)})}\sigma_{33}^{(k,l)}(x_n,x_t,0), \\ K_2(x_t) &= \lim_{x_n\to 0}\sum_{l=1}^{3}\sum_{k=1}^{6}(\sqrt{2\pi})x_l^{(1-\lambda^{(l)})}\tau_{n3}^{(k,l)}(x_n,x_t,0), \\ K_3(x_t) &= \lim_{x_n\to 0}\sum_{l=1}^{3}\sum_{k=1}^{6}(\sqrt{2\pi})x_l^{(1-\lambda^{(l)})}\tau_{3t}^{(k,l)}(x_n,x_t,0) \end{aligned} \right. \tag{14}$$

are used, where $\sigma_{33}^{(k,l)}$, $\tau_{n3}^{(k,l)}$ and $\tau_{3t}^{(k,l)}$ are calculated from the edge eigen functions and the calculated complex stress intensity functions associated with Eq. (13). The first and second summation refer to the three singular eigen functions and the six Lekhnitskii functions with complex variables. The definition for the stress intensity factor in Eq. (14) was introduced by Wang and Choi (1982). By the virtue of the complex conjugacy of the singularity exponents, the stress intensity factors are uniquely defined real quantities.

Another, and perhaps more consistent approach, is to introduce a length, r_0. Complex stress intensity factors complemented with such a length fully characterize the stress field at the crack tip (Rice, 1988). By this approach, the phase angle can be interpreted as, $\psi = \mathrm{atan}(\tau_{3n}/\sigma_{33})$ at this point. Fracture toughness data must then be defined for the same length.

The STRIPE analysis provides the complete analysis including the oscillatory stresses. All three approaches for the definition of stress intensity factors can therefore be adopted. In most practical situations (unless a very small r_0 is used), the difference in the resulting phase angle from the three alternatives is small. It should also be kept in mind that there are no distinct interfaces in composite materials (as in the mathematical problem), which could be another argument to ignore the oscillations. In fact, in the 'composite world', mode mixity is usually described as energy release rates and fundamental problems related to oscillatory stresses are ignored.

In the simulations of delamination growth below, an approximate mode decomposition will be used. Stress intensity factors related to the in-plane loads N_{nn} and M_{nn}, will be calculated using Eqs. (10) and (11). The contribution from the shear force, Q_n, will be assumed pure mode I loading. This assumption is based on results from the reliable finite element analysis outlined below and will be demonstrated in the results section. The stress intensity factors may then be written as

$$\begin{cases} K_{\mathrm{I}} = K_{\mathrm{I}}^{\mathrm{iso}} + K_{\mathrm{I}}^{Q}, \\ K_{\mathrm{II}} = K_{\mathrm{II}}^{\mathrm{iso}}. \end{cases} \tag{15}$$

The shear force stress intensity factor, K_{I}^{Q}, is taken as,

$$K_{\mathrm{I}}^{Q} = \sqrt{E_{nn} G_{Q}}, \tag{16}$$

where E_{nn} is the "effective" Young's modulus of the delaminated member in the direction normal to the front and G_Q the contribution to the energy release rate from the shear forces. A negative K_{I} would indicate that the crack tips overlap locally. Such an overlap is not physically feasible and when that occurs we assume that the crack tip loading becomes pure mode II, i.e.,

$$\begin{cases} \psi = \operatorname{atan}(K_{\mathrm{I}}/K_{\mathrm{II}}) & K_{\mathrm{I}} \geqslant 0, \\ \psi = 90^{\circ}\operatorname{sign}(K_{\mathrm{II}}) & K_{\mathrm{I}} < 0. \end{cases} \tag{17}$$

3. Numerical procedure

The test panels have been analysed with the structural model described above using four-noded (degenerated) isoparametric shell elements implemented in the commercial FE-code ADINA. A plane projection of the adopted FE mesh with applied boundary and symmetry conditions is shown in Fig. 4. The same mesh has been adopted for the lower and upper part. The plies above and below the delaminated interface are modelled as separate shell elements with constraint and contacts conditions described above. Each of these are modelled as layered shells with the given layup sequence and stiffness properties.

The displacement field of the lower plate element layer in the undelaminated domain is constrained to the upper plates nodewise by relation (4). The contact condition (5) is implemented nodewise and in an approximate way. Nodes in the upper and lower part of the delaminated region with the same inplane coordinates are joined by a linear elastic spring with spring stiffness, which for the ith node pair is given by

$$K_i = 2A_i E_{33}/(t+T), \tag{18}$$

where K_i replaces S and σ_N is replaced by contact forces R_i. A_i denotes the area coupled to the node (the sum of all A_i equals the delaminated area). These 'contact' springs have a 'death–birth option', which makes it possible to assign zero spring stiffness outside the contact zone and to activate and de-activate contact nodes as the contact area changes. The relative transverse displacement, Δu_3 in Eq. (5) is replaced by the contact spring elongation, d_i. Thus, the contact pressure is different from zero when the contact spring is shortened. Since we base the contact on the spring shortening instead of the true relative transverse deflection, we assume that the out-of-plane component of the relative displacement is substantially larger than the in-plane displacements. The contact zone and contact forces are computed by a predictor correction method where springs in tension become inactive and springs between node pairs where interpenetration occurs become active. The contact analysis has converged when the two convergence conditions

$$\sum_{i=1}^{N-N_{\mathrm{c}}} \left(1 - \frac{d_i}{|d_i|}\right) \leqslant \varepsilon_d, \qquad \sum_{i=1}^{N_{\mathrm{c}}} \left(1 - \frac{R_i}{|R_i|}\right) \leqslant \varepsilon_R \tag{19}$$

are fulfilled. N is the number of nodes in the delaminated region and N_{c} the number with active contact springs. N_{c} has to be determined as part of the nonlinear solution. Both criteria are used when contact is partial (this was the case in all numerical examples below). When there is full contact, then only the force criterion is used, whereas when there is no contact, only the displacement criterion is used. In these two special cases, the criteria are fulfilled exactly. In the present investigation, $\varepsilon_d = 10^{-3}$ and $\varepsilon_R = 10^{-2}$ were used. This contact model is very similar to what has been recently proposed by Kyoung et al. (1999).

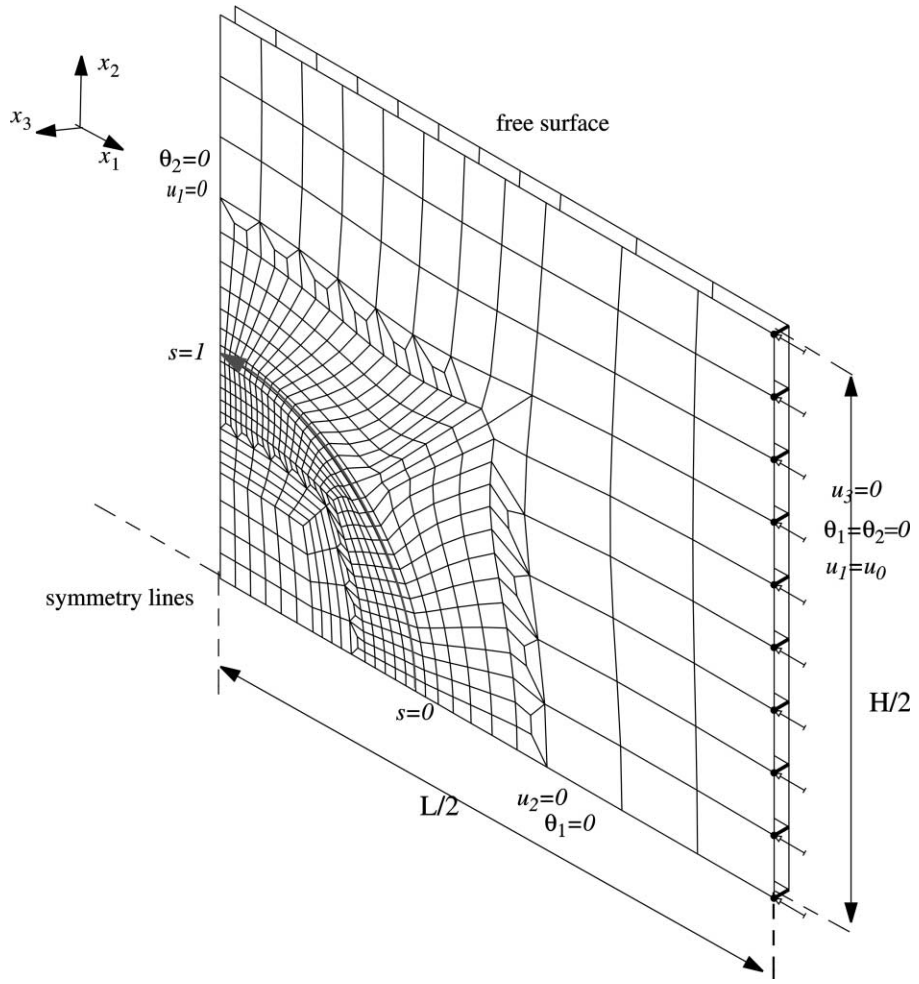

Fig. 4. FE mesh used in the analyses at initial growth and applied boundary and symmetry conditions.

The main difference between the present global bending and thin film contact model described in Giannakopolous et al. (1995) is that here both plates deflect and the contact area is not a flat surface. The contact algorithm in the thin film case, which was based on the true transverse deflection, Δu_3, is discussed in some detail in Giannakopolous et al. (1995).

A complete analysis of delamination buckling and growth includes the following steps:

(1) The global (plate) buckling load is first determined for the structure by imposing constraint (4) in the delaminated region and performing the eigenvalue analysis.

(2) The delamination buckling load is subsequently determined with due account to contact at buckling following the contact procedure outlined above.

(3) This is followed by the kinematically nonlinear post-buckling analysis where the full Newton method is adopted and where the contact analysis is performed at each load. Once the contact analysis has converged, the energy release rate is computed along with fracture mode separation (i.e. Eqs. (10)–(12) and (15)–(17)). Load increments are taken automatically such that load increments are small at the delamination and global buckling load where the tangential stiffness may be very low. Load increments are also

adjusted such that the crack growth criterion is attained without significant violation. In the numerical analyses given here, the energy release rate was within 1% of the critical value at crack growth.

(4) The front may propagate when the crack growth criterion, $G(\psi) = G_c(\psi)$, has been attained at some node. The front is then advanced by moving the nodes that have reached the crack growth criterion a small (see below) distance in the local normal direction to the front and in the plane of the delamination, followed by a step where the entire mesh is slightly moved. The post-buckling analysis is then restarted at the previous propagation load, but with the new updated mesh.

By this approach, the evolution of the delamination growth is modelled by performing a large number (typically in the order of a few hundred) of incremental crack propagations. The "small" distance the nodes are propagated must be finite but sufficiently small. Large values may induce spurious variations in the energy release rate distribution along the part of the front that propagates. In the analysis below, the maximum crack increment was 0.25% of the delamination radius. This value has been determined from numerical experiments and gives virtually no spurious variation in the energy release rate along the part of the front that propagates as we will exemplify later. The moving mesh part is done by solving a two-dimensional finite element problem using the same mesh as in the shell analysis. Nodes along the delamination front, which have attained the crack growth criterion, have prescribed displacements equal to the crack increments. Nodes along the front, which have not attained the crack growth criterion and nodes along the outer boundary, have zero prescribed displacements. The new nodal coordinates for the shell problem are taken as the nodal coordinates after deformation of this two-dimensional problem. A more detailed description of the moving boundary technique can be found in Nilsson and Giannakopoulos (1995).

4. Experimental methods

4.1. Test specimens

Carbon fibre/epoxy laminates with an implanted artificial delamination were tested. A cross-ply layup $[(90°/0°)_{17}/90°]$ was chosen, where the 0°-direction was parallel to the x_1 direction (Fig. 5). Delamination growth was expected in the x_2 direction, i.e. perpendicular to the applied load. Growth in this direction was bounded by parallel fibres, which prevented out-of-plane kinking of the crack. The laminates were manufactured from toughened resin HTA/6376C prepreg, manufactured by Hexcel. The laminates were cured according to the manufacturer's recommendations. The mechanical properties of the unidirectional lamina in compression were $E_{11} = 131$ GPa, $E_{22} = 11.7$ GPa, $E_{33} = 11.7$ GPa, $G_{12} = G_{13} = 5.2$ GPa, $G_{23} =$

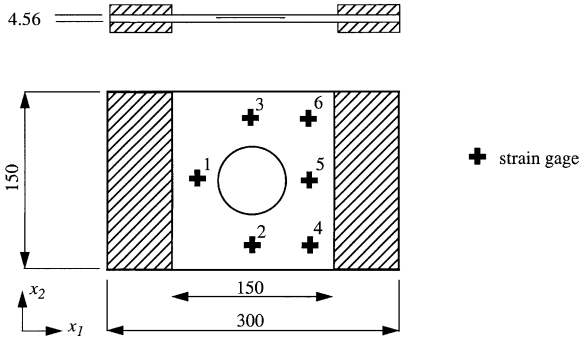

Fig. 5. Schematic top and side view of the delaminated composite plate (lengths in mm).

3.9 GPa, $v_{12} = v_{13} = 0.3$ and $v_{23} = 0.50$. The nominal ply thickness of each ply was 0.13 mm. The measured thickness of the laminates was 4.58 mm with a standard deviation of 0.03 mm.

All specimen dimensions are presented in Fig. 5. To evaluate uniformity of uniaxial loading, all plates were instrumented with 0°/90° strain gauges. In total, six strain gauges were bonded on each face of the plates, Fig. 5. Panels with no delamination and panels with an artificial delamination inserted after prepreg layers three, five or seven, respectively ($N = 3, 5, 7$) were manufactured.

The specimens came from two test series with 12 and 14 panels respectively. The first test series has been described in Nilsson et al. (1997). In an earlier study, the insert thickness was found to influence the fracture toughness at initiation (Olsson et al., 1996). In the first test series, delaminations were therefore created by inserting two 7.5 μm thin, stacked circular polyimide films with diameters 55 and 60 mm respectively. To prevent adhesion, a thin layer of Teflon was sprayed between the two polyimide films. Still in several tests the two films did not separate properly. To alleviate this problem, the insert in the second test series was replaced by a single 25 μm thick circular Teflon film with a 60 mm diameter.

The pressure in the enclosed volume of artificially embedded delaminations and manufacturing defects could be lower than ambient pressure. This pressure difference could suppress delamination buckling. The extensive matrix cracking seen in impact damage would probably eliminate such a pressure difference. To achieve a similar effect in the test, a hole with a 1.2 mm diameter was drilled in the centre of the delamination and through the substrate. To simulate a manufacturing defect, a few panels were tested undrilled.

The critical energy release rate depends strongly on the mode mixity. The mixed mode critical energy release for the present material was determined by Juntti et al. (1999) from the mixed mode bending (MMB) test. Specimens with a layup $[0°_{12}//(\pm 5°/0°_4)_s]$ was used in these tests, where the sign "//" refers to the plane of the delamination. The off-axis angle was applied to reduce fibre bridging at delamination growth.

The mixed mode fracture toughness can for most materials be accurately described by a three-parameter relation, $G_C(G_{IC}, a_1, \lambda; \psi)$, where

$$\begin{cases} G_C = G_{IC}[a_1 f_1(\psi, \lambda) + (1 - a_1) f_2(\psi, \lambda)], \\ f_1(\psi, \lambda) = 1 + \tan([1 - \lambda]\psi)^2, \\ f_2(\psi, \lambda) = \frac{1}{1 + (1 - \lambda)\sin(\psi)^2}. \end{cases} \tag{20}$$

The three parameters for a specific material, (G_{IC}, a_1, λ), are determined by fitting Eq. (20) to test results. The functional forms f_1 and f_2 have been suggested by Hutchinson and Suo (1992). The experimentally determined mixed mode fracture toughness and $G_C(G_{IC}, a_1, \lambda; \psi)$ with $G_{IC} = 250$ J/m^2, $\lambda = 0.22$ and $a_1 = -0.10$ are plotted in Fig. 6. We see that this choice of the parameters gives a snug fit with the test results.

4.2. Test procedure

The plates were loaded in an MTS servo-hydraulic load machine with a maximum load capacity of 250 kN with manual displacement control. In all tests, the load was applied in the x_1 direction at ambient conditions. As will be discussed further below, the machine clamping used for the reference plates in the first test series was insufficient to achieve the clamped boundary conditions given in Fig. 4. Steel plates were therefore bonded on to all composite plates tested in the second test series by a room temperature curing adhesive and cured for a minimum of 48 h. The influence of clamping conditions will be discussed in detail below.

Instrumented dial gauges measured out-of-plane displacements in the centre of the composite plates. However, as will be discussed in Section 5, the point load of the dial gauge affected the buckling of the delaminated member. Noncontact displacement measurements of the out-of-plane displacement were

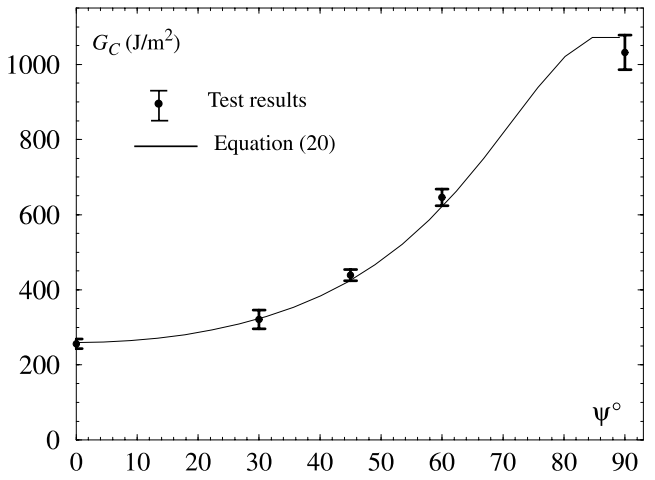

Fig. 6. Critical energy release rate as function of phase angle determined from MMB test and fitted curve with $G_{IC} = 250$ J/m^2, $\lambda = 0.22$ and $a_1 = -0.10$ in Eq. (20).

therefore utilized in the tests of five plates ($N = 3, 7$). The noncontact measurements were performed on the delaminated side of the plates by a laser instrument. A spectra-MS data acquisition system was used to record load, in-plane and out-of-plane displacements and strain gauge responses. Acoustic emission (AE) was employed to detect initiation of delamination growth using a Locan 320 system and a R15 transducer with a resonance frequency of 175 kHz.

The plates were scheduled to be tested in the following sequence: In the first load step, delamination buckling load of the initial delaminated region was determined. In the second load step, or in the continuation of the first load step, the plates were loaded until global buckling or initial delamination crack growth took place, whichever occurred first. In the case of stable delamination growth, the second load step was repeated to achieve another growth increment. In the third and final step, the plates were loaded until failure. To monitor possible delamination crack growth, the plates were dismounted and analysed by ultrasonic C-scan after each load step.

5. Results

5.1. Experimental results

The experimental results for the plates in test series 1 and 2 are presented in Tables 1 and 2, respectively. In Table 1, superscripts a and b refer to two different clamping conditions, where a is machine clamping of the composite plate with a free length of 145 mm and superscript b refers to steel plates adhesively bonded to the plate and a free length of 150 mm. Table 2 gives data for specimens that were bonded to steel plates (with a free length of 150 mm). Superscript a in Table 2 refers to undrilled specimens whereas superscript b refers to out-of-plane displacement measurements by a noncontact laser instrument instead of a dial gauge. The specimen labelling in Tables 1 and 2 give information of the position of the delamination, specimen number and load step respectively. For instance A3_6_1 relates to the *first* load step of the *sixth* specimen with a delamination after the *third* layer, $N = 3$.

The labelling P_{DB} and P_{GB} refer to "delamination" and "global" buckling respectively. Due to geometrical imperfection, and to a lesser extent by nonsymmetry of the delaminated plate, there is not nec-

Table 1
Experimental results of the delaminated plates with two 7.5 μm polyimide inserts

Specimen number	P_{DB} (kN)	$P_{GB} = P_M$ (kN)	P_{growth} (kN)	Δa (mm)
Aref_1[a]	_1: none	110.6 (P_{GB})	None	None
Aref_2[a]	_1: none	113.5 (P_{GB})	None	None
A3_1[a]	_1: 110.5	110.5	110.5	5
	_2: 12.3	110.7	109	2
	_3: 19.1	112.4	110	Failure
A3_2[a]	_1: 115.0	115.0	115	7.5
	_2: 10.3	110.4	109	1
	_3: 11.5	110.8	109	Failure
A3_3[a]	_1: pert.	pert.	pert.	6
	_2: 12.6	108.7	108	1
	_3: 12.4	108.9	108	Failure
A3_4[b]	_1: 19.4	106.9	None	None
	_2: 17.2	106.4	106.4	6
	_3: 14.3	109.6	109.6	Failure
A3_5[b]	_1: pert.	pert.	pert.	4
	_2: 26.2	104.3	104.3	0.5
	_3: 26.6	108.7	108.7	3
A5_1[b]	_1: 61.3	107.8	107.8	Failure
A5_2[b]	_1: pert.	117.0	pert.	20.2
	_2: 57.3	100.7	100.7	Failure
A7_1[a]	_1: pert.	pert.	pert.	None
	_3: 96.1	110.6	110	8
	_6: 66.8	110.2	110	Failure
A7_2[a]	_1: pert.	115.2	pert.	3.5
	_2: 98.4	111.2	110	3.5
	_3: 75.4	110.1	109	Failure
A7_3[a]	_1: pert.	106.3	pert.	7.5
	_2: 63.3	108.3	108	2.5
	_3: 61.3	107.3	107	Failure

essarily a bifurcation point. The term "buckling" has been used for convenience. The delamination buckling load, P_{DB}, is defined as the load where onset of a nonlinear relation between the applied load and the transverse deflection of the delaminated member is observed. The global buckling load, P_{GB}, is defined as the first load at which the out-of-plane displacement of the substrate increases at constant load, i.e. zero post-buckling stiffness. P_M refers to the maximum load sustained by the panel. P_{growth} is the load at delamination growth and Δa is the subsequent incremental delamination growth at each load step in mm. Δa was determined as the average growth in the two delamination growth regions, with exceptions for highly unsymmetric cases for which the growth in each region is given. Delamination buckling at the first step was difficult to achieve in many panels in the first test series where the delamination did not open properly. In such cases, an out-of-plane perturbation load was applied manually at high compression load (typically close to global buckling load) to open the delamination. The perturbed plates are indicated by the abbreviation pert. in Table 1.

Table 2
Experimental results of the delaminated plates with 25 μm Teflon insert

Specimen number	P_{DB} (kN)	$P_{GB} = P_M$ (kN)	P_{growth} (kN)	Δa (mm)
Aref_3	_1: none	115	None	None
Aref_4	_1: none	115	None	None
A3_6[a]	_1: 29	105	105	10
	_2: 22	106	106	15
	_3: 11	105	105	Failure
A3_7[a]	_1: 22	106	106	3
	_2: 19	114	–	None
	_3: 17	113	Failure	Failure(i)
A3_8[a]	_1: 24	99	99	4
	_2: 15	105	105	10
	_3: 6	104	104	Failure
A3_9	_1: 15(ii)	–	–	None
	_2: 30	106	106	8
	_4: 7(ii)	–	–	None
	_5: 13	105	104	1.5
	_6: 13	–	–	5
	_7: 11	104	103	Failure
A3_10[b]	_2: 11	104	103	6
	_3: 10	108	108	7
	_4: 9	107	107	13
A3_11[b]	_2: 8	105	104	8
	_3: 6	105	104	2.5
	_4: 5	105	104	16
A5_3	_1: 45	–	–	None
	_2: 46	106	106	20 & 35
	_3: 26	102	102	1
A5_4	_1: 39	–	–	None
	_2: 37	107	107	20 & 35
	_3: 22	104	104	25 (to left edge) & 5
A5_5	_1: 40	–	–	None
	_2: 40	108	108	24 and 45 (to right edge)
A7_4[b]	_1: 71(iii)	102	101	11.5
	_2: 51	103	102	1.5
	_3: 38	102	102	Failure
A7_5[b]	_2: 72	105	104	10.5
	_3: 51	103	–	None
	_4: 51	104	103	5
A7_6[b]	_2: 68	103	102	15
	_3: 36	103	103	Failure

(i) Failure was not caused by delamination growth. (ii) Refers to true loads for onset of local nonlinearity, dial gauge force cancelled (case C, Fig. 7). (iii) The delamination buckling was initiated by introduction of a point load.

No data of the in-plane displacements is provided in Tables 1 and 2, since the cross-head displacement measurements in the load frame had an accuracy of only 0.1 mm, whereas the imposed end-displacements were of order 0.5 mm.

Prior to global buckling and delamination growth, the discrepancy between the strain gauge couple 2 and 3, (Fig. 5) was less than five percent, which indicated a rather symmetric strain distribution, which motivated modelling of only one quarter of the plates. At extensive delamination growth, however, symmetry was lost and the difference in measured strains could be more than 50%. Strain gauge couples 1 and 5, and 4 and 6, were affected by the clamping and symmetry assumptions and could therefore not be evaluated.

5.1.1. Global buckling and maximum load

As shown in Tables 1 and 2, the global buckling load, P_{GB}, equalled the maximum compressive load, P_M, in all plate tests. Consequently, no increase in stiffness was observed in the post-buckling regime. The maximum load of the undelaminated plates was 110–115 kN. The average maximum load for delaminated panels was slightly lower but virtually unaffected by delamination depth; the measured loads in the second series were 104, 107 and 103 kN for the A3, A5, and A7 plates, respectively. The average of maximum load for all delaminated plates in the second series was 105 kN with a standard deviation of 3 kN, only. Thus, an excellent repeatability in the maximum load was achieved in the tests. The load versus out-of-plane displacement for the two undelaminated plates as well as for three delaminated plates are shown in Fig. 7. All plates show very similar behaviour. The main difference lies in the 10% drop in the maximum load for delaminated plates compared to undelaminated ones. This difference may be explained by the alteration in failure mode; the artificially delaminated plates failed by delamination growth whereas undelaminated plates failed in compression at global buckling.

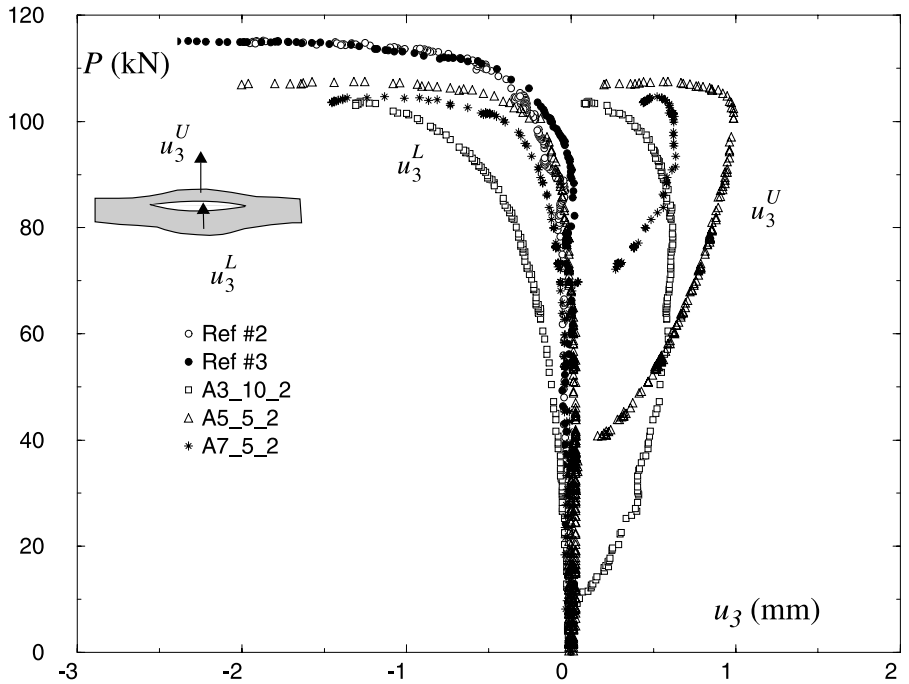

Fig. 7. Measured load versus out-of-plane displacement at lower, u_3^L and upper u_3^U side of panel of undelaminated and delaminated plates.

5.1.2. Delamination buckling and out-of-plane displacements

Two particular aspects, which we anticipated might influence the delamination buckling load, were studied in more detail; the pressure inside the delamination (panels with and without drilled hole) and the restraining effect from dial gauge, which exerts a load of approximately 1 N on the delamination. The transverse load necessary to restrain out-of-plane deflection is relatively small, in particular for thinner delaminations. The force exerted by the dial gauge may therefore suppress delamination buckling. Four different test conditions, which we label A–D (see Fig. 8) were studied:

- Test Condition A: the panel was undrilled and a dial gauge was applied on the delaminated member;
- Test Condition B: a hole was drilled through the substrate but the dial gauge was applied as in test condition A;
- Test Condition C: the drilled hole was retained, but now two dial gauges, one on each side of the delaminated member to cancel a resulting force, were applied on the delaminated member;
- Test Condition D: the dial gauge on the delaminated member was replaced by a noncontact laser instrument.

The measured delamination buckling loads for different delamination depths and test conditions A–D are given in Fig. 8. Panels with improper separation have been excluded. The same panels were used for Test conditions B and C. Due to the limited number of tests no definite conclusions can be drawn. However, the following trends can be clearly seen:

- the delamination buckling load for the three layer delamination ($N = 3$) is not increased (it is even lower) for test condition B compared with test condition A. Hence, there is no enclosed vacuum that inhibits

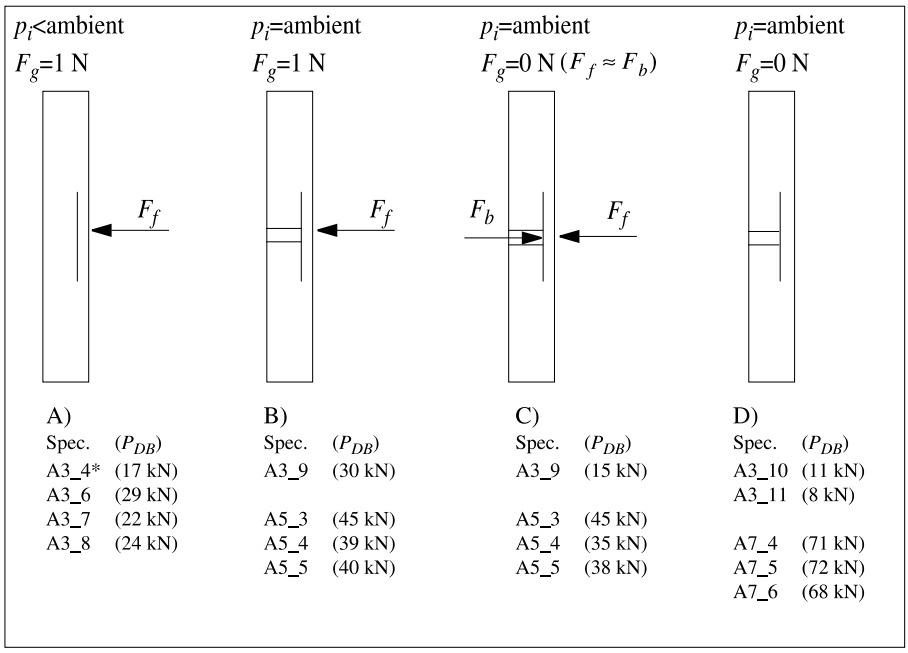

Fig. 8. Schematic illustration of the four test conditions A–D. F_g refers to the total resulting gauge load acting on the delaminated member.

buckling in undrilled panels. Therefore, the drilled hole has only a marginal effect on the buckling of thin delaminated members;

- a comparison between test conditions B and C indicates that a resultant dial gauge force has a distinct effect on the delamination buckling load for the three-layer delamination, whereas the effect is virtually negligible for the thicker five-layer delamination;
- in test condition D, the delamination buckling load for the three-layer delamination is reduced even further, which indicates that the dial gauge pair in test condition C did not completely eliminate the dial gauge effect.

It is worth noting that the delamination buckling load was not very distinct in many panels and that the three-layer delamination panels with Teflon inserts had a rather strong imperfection behaviour.

The specimens that reliably mimic the case of buckling and delamination growth in the tests are identified as the A3 and A7 plates tested in D, as well as the A5 plates tested in B (and C). The complete load–displacement curves from tests on these plates are depicted in Fig. 9a–c. As already mentioned, a clear

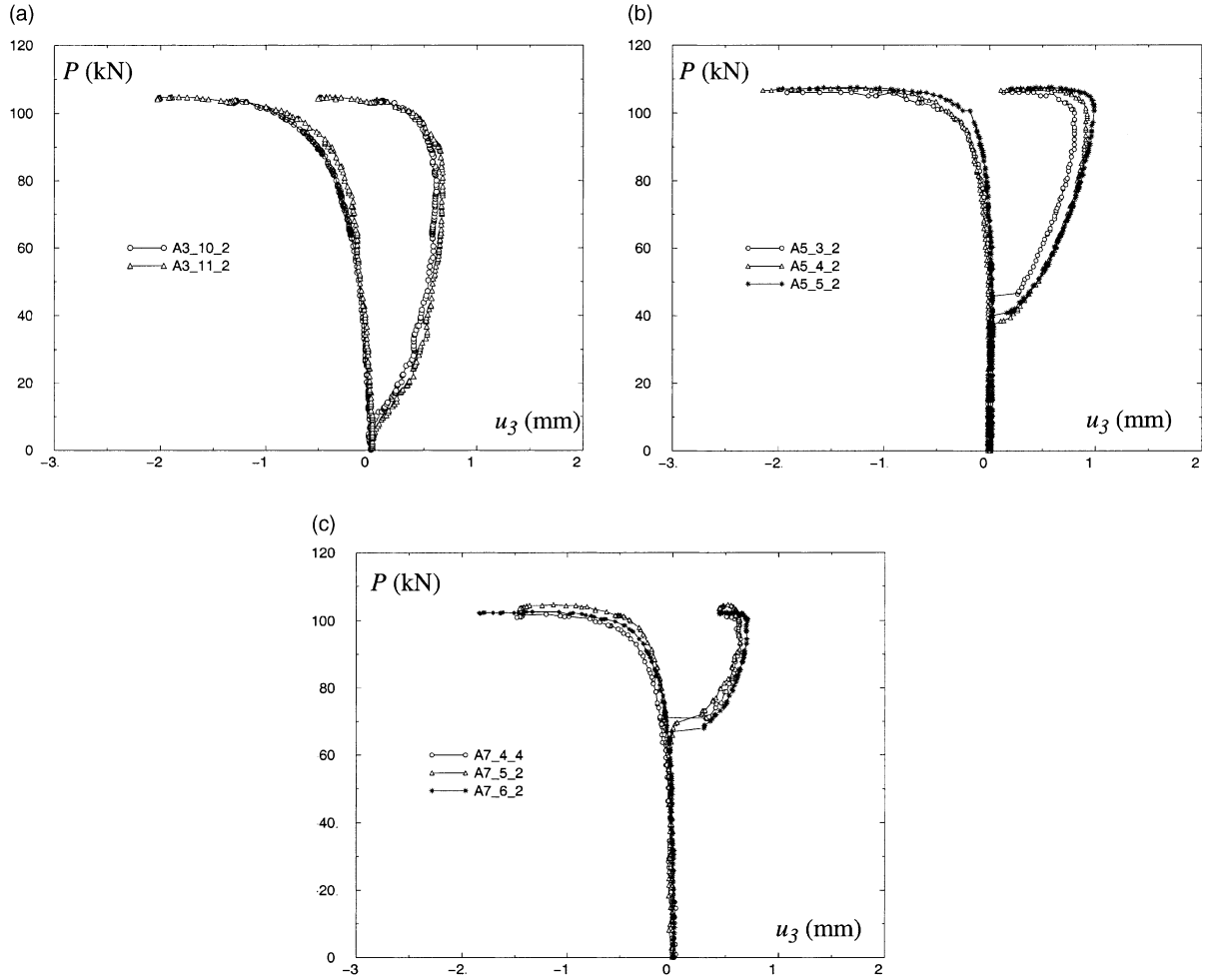

Fig. 9. Load–displacement curves for plates delaminated after (a) three layers, (b) five layers and (c) seven layers.

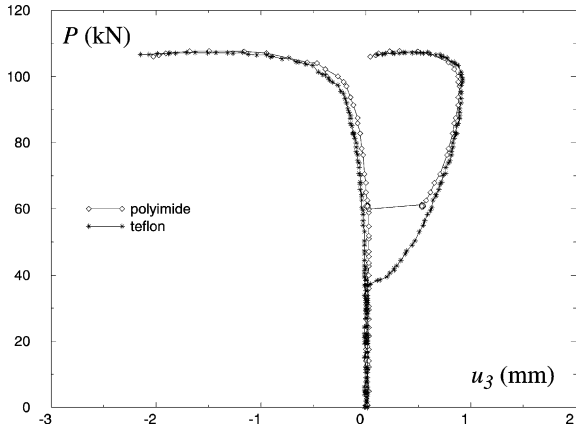

Fig. 10. Experimentally determined load–displacement behaviour of plates A5_1 and A5_4.

imperfection behaviour for the three-layer delaminations was observed with Teflon inserts. These panels were all cut from one big panel and it is more likely that the imperfections were caused by a slight curvature of this plate than by the inserts. As shown in Fig. 9a–c, the load at delamination buckling increased as expected with the thickness of the delaminated member. For A3 plates, the delamination buckling load was about 10 kN, whereas the average loads at delamination buckling of the A5 and A7 plates were approximately 40 and 70 kN, respectively. The load–displacement curves in Fig. 9a–c show an excellent repeatability in compression behaviour of the plates, up to global buckling and delamination growth and with small or no delay in the out-of-plane displacement at delamination buckling. This was not the case with polyimide inserts as shown in Fig. 10, where the delamination buckling was delayed compared to that with a Teflon insert. However, as also seen in Fig. 10, after delamination buckling, the out-of-plane displacements of the plates were almost identical. Ultrasonic C-scans of the two types of artificial delami-

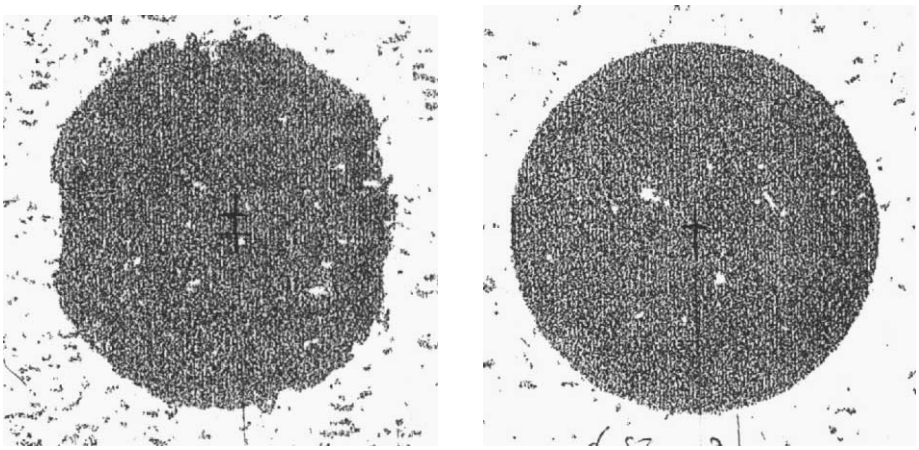

Fig. 11. C-scans of the two artificial delaminations used: (a) stacked polyimide films and (b) single Teflon film.

nations presented in Fig. 11 indicate significant adhesion between the stacked polyimide films and the composite, whereas no adhesion is observed in the case of a Teflon insert. Adhesion between the stacked polyimide films and the composite was also confirmed by cutting one panel with each insert open. The polyimide films were strongly bonded to the composite, whereas the Teflon film was easily removed by a pair of tweezers.

As a result of the eliminated adhesion in the second test series, delamination buckling at the first load step occurred in all plates with the exception of plate A7_4. For this plate, a very small point load, applied through the drilled hole by a touch of a needle, was needed to make the delamination snap and buckle outwards. Due to the improved delamination conditions with Teflon inserts, the scatter in data was reduced significantly and the repeatability of the load at delamination buckling was improved.

5.1.3. Delamination growth

Delamination growth initiated at or slightly below global buckling in all specimens. In all tests, the delaminations grew more or less symmetrically and perpendicular to the direction of load. Fig. 12 shows one of the two delamination growth regions after 7 and 8 mm growth in an A3 and an A7 plate, respectively. The figure shows that the growth is more localized in the plate with a thin delaminated member. This trend was observed in all specimens. Consequently, A7 plates exhibited the widest delamination growth regions and A3 plates the most narrow growth regions.

The plates were cut open for post-mortem analysis of the delamination growth regions. The fractographical results showed that delamination growth occurred in mixed mode I and mode II conditions in the entire growth regions. Independent of the thickness of the delaminated member, shear cusps and ribs were found in the initiation region, which implied presence of a mode II component at initiation of delamination growth. Fig. 13 presents scanning electron microscope (SEM) micrographs of the delamination growth region for a plate with a delamination after three layers. The frequent appearance of shear cusps and ribs in the delamination growth region and in the direction of major growth (Fig. 13a,b), i.e. perpendicular to the load direction, indicates prevailing mixed mode I and mode II conditions. No conclusive fractographic evidence could be found that suggest a change in the mode mixity in the major growth direction. Nevertheless, observations of an increase in the amount of broken fibres indicate that this may yet be the case.

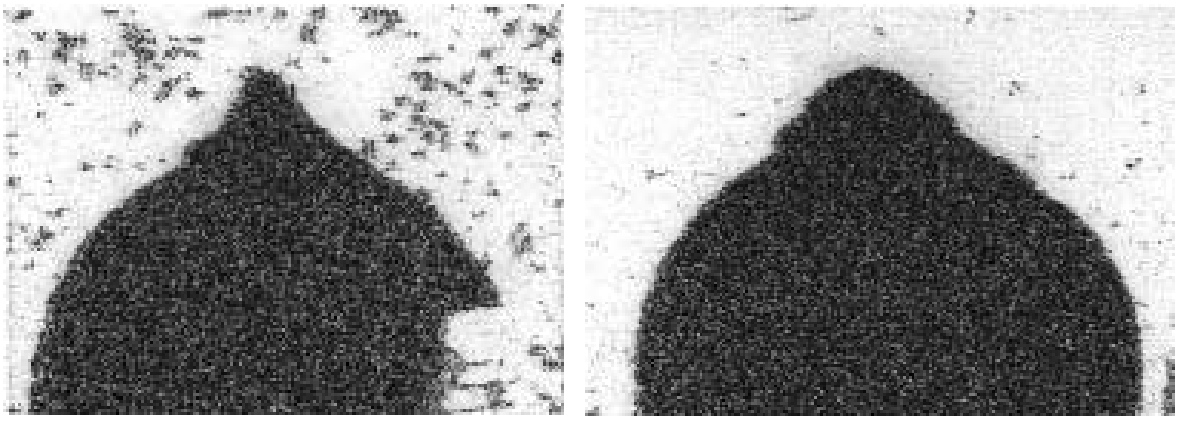

A3_4 at 7 mm growth A7_1 at 8 mm growth

Fig. 12. Ultrasonic C-scans of three- and seven-layer delaminations. Loading from left and right.

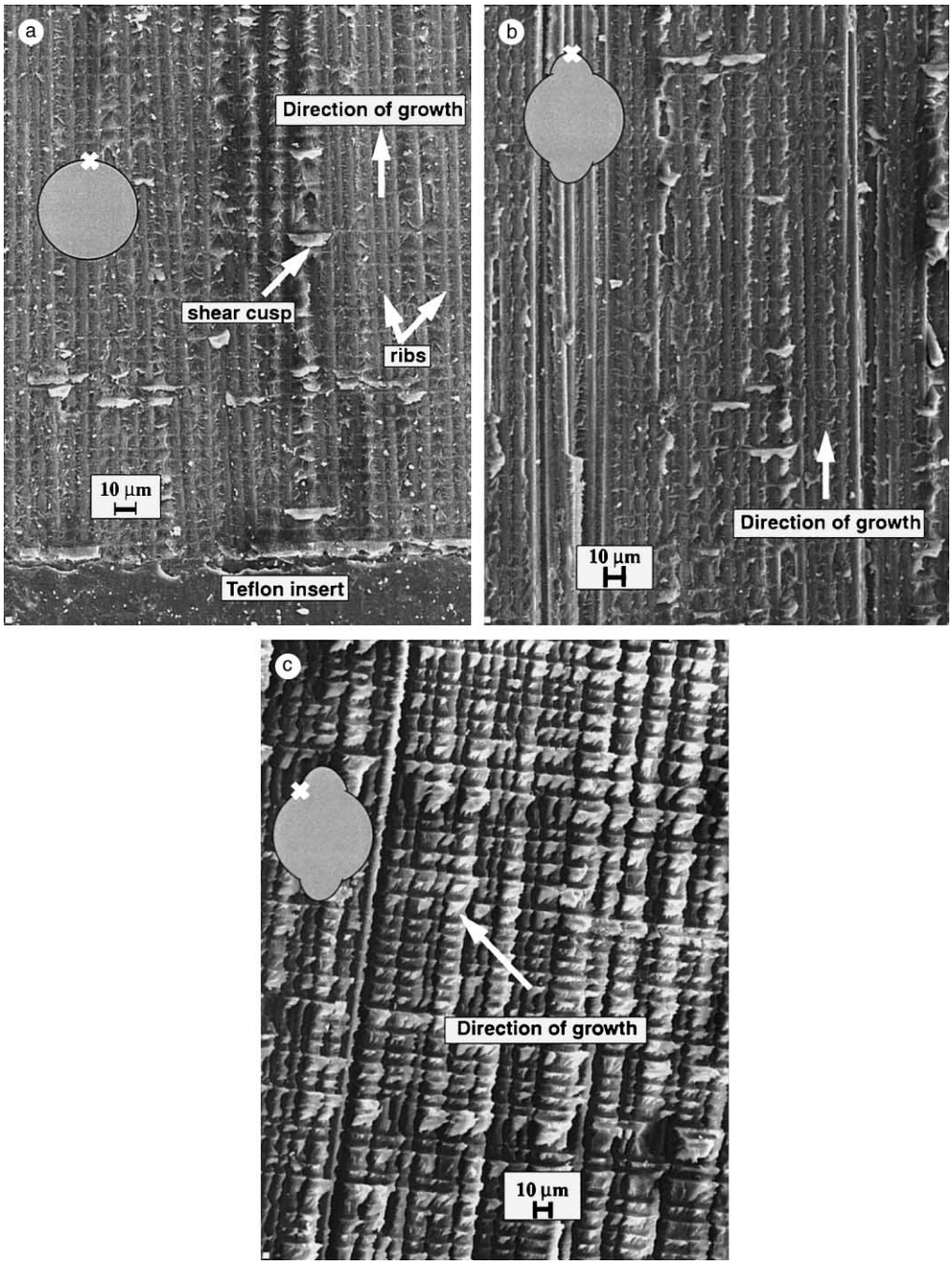

Fig. 13. SEM micrograph for three-layer delaminations at three different locations given in the inset: (a) at initiation region perpendicular to applied load (b) at 8 mm of growth perpendicular to applied load and (c) incipient growth at an angle to fibres.

Further fractographic studies are required to investigate this. Fig. 13c shows the fracture surface close to the Teflon insert away from the initiation region. The depicted micrograph shows mode II dominated

growth at an angle to the fibre direction of the upper ply. This conclusion is based on the massive amount of shear cusps and their inclination which is a manifestation that the mode mixity changes within the growth region.

The loading was controlled manually with virtually constant load increment until indication of delamination growth when further loading was stopped. Loading up to onset of delamination growth took about 1 min. The actual time from the indication of delamination growth until the loading was stopped was typically a couple of seconds. Since the load increment is constant, additional displacement after onset of delamination growth was only a fraction of the total applied displacement. We see from Tables 1 and 2 that only one panel, A_5, failed already at first delamination growth. For all other panels, delamination growth ranged from just a few mm up to 35 mm, which indicates a semi-stable growth under controlled displacement loading. In the final load step a shift to unstable growth during delamination propagation was observed in most of the A5 and A7 plates. Thus, the results indicate a shift in the stability of the delamination growth as the thickness of the delaminated member increases.

5.2. Assessment of approximate mode separation

In the simulations of the panel tests below, the approximate mode decomposition defined by Eqs. (10)–(12) and (15)–(17) was adopted. This approximate mode separation should only be used if the resulting phase angle is sufficiently close to the phase angle given by a complete and reliable analysis of the layered and anisotropic material.

To verify this the phase angle was computed using the approximate mode decomposition and the full FE analysis of the layered and anisotropic material with stress intensity factors defined by Eq. (14). In the reliable finite element analysis, the material data given above were used with the layup sequence $[(0°/90°)_{17}/0°]$, which corresponds to growth orthogonal to the load direction. For this particular layup, the mode III loading is decoupled from the mode I and mode II loadings, and the plain strain conditions can be used in the finite element analyses. In the finite element, each ply was modelled separately with a very refined mesh at the crack tip. The analyses were done with polynomial orders 2, 3, 4 and 5. By this procedure, it was possible to assess the numerical accuracy of the results. The difference in the computed stress intensity for $p = 4$ and 5, then gives a direct measure of relative numerical error in the computed phase angle. The error was less than 10^{-3}, for the results to be presented.

The phase angles versus the delamination depth for the three load cases: in-plane membrane load; in-plane bending load; in-plane shear load are depicted in Fig. 14a–c respectively. The three depths where delaminations were inserted in the tests are marked with 3, 5 and 7. For the shear force load case, a moment couple, $Q_n l$, where l is the crack length in the FE model has been introduced to eliminate the length effect in the computed phase angle. The most important observation is that, except for the case with delamination after two plies, the phase angle given by the full and the approximate decomposition are very similar. The large error for the second ply delamination is not surprising since the stress distribution in the thin member differs significantly from the isotropic case, but as we may see from Fig. 14, this effect is drastically reduced when the delamination is deeper and the layup effect smeared out. It may also be noted from Fig. 14, that for the membrane load case and the shear load case, there is a consistent difference when the delamination is located in the 0°/90° and 90°/0° interface. The imaginary part of the singular exponents, ε was 0.03 for these layups, which indicates a small region with oscillatory stresses.

Analyses, similar to those given in Fig. 14, can be performed for growth in other directions. However, in the general case, all three fracture modes will be coupled and generalized plane strain conditions need to be imposed (see Nilsson et al. (2000)). As long as the growth is primarily orthogonal to the load, we will surmise that the approximate mode separation is relatively accurate for the three delamination depths.

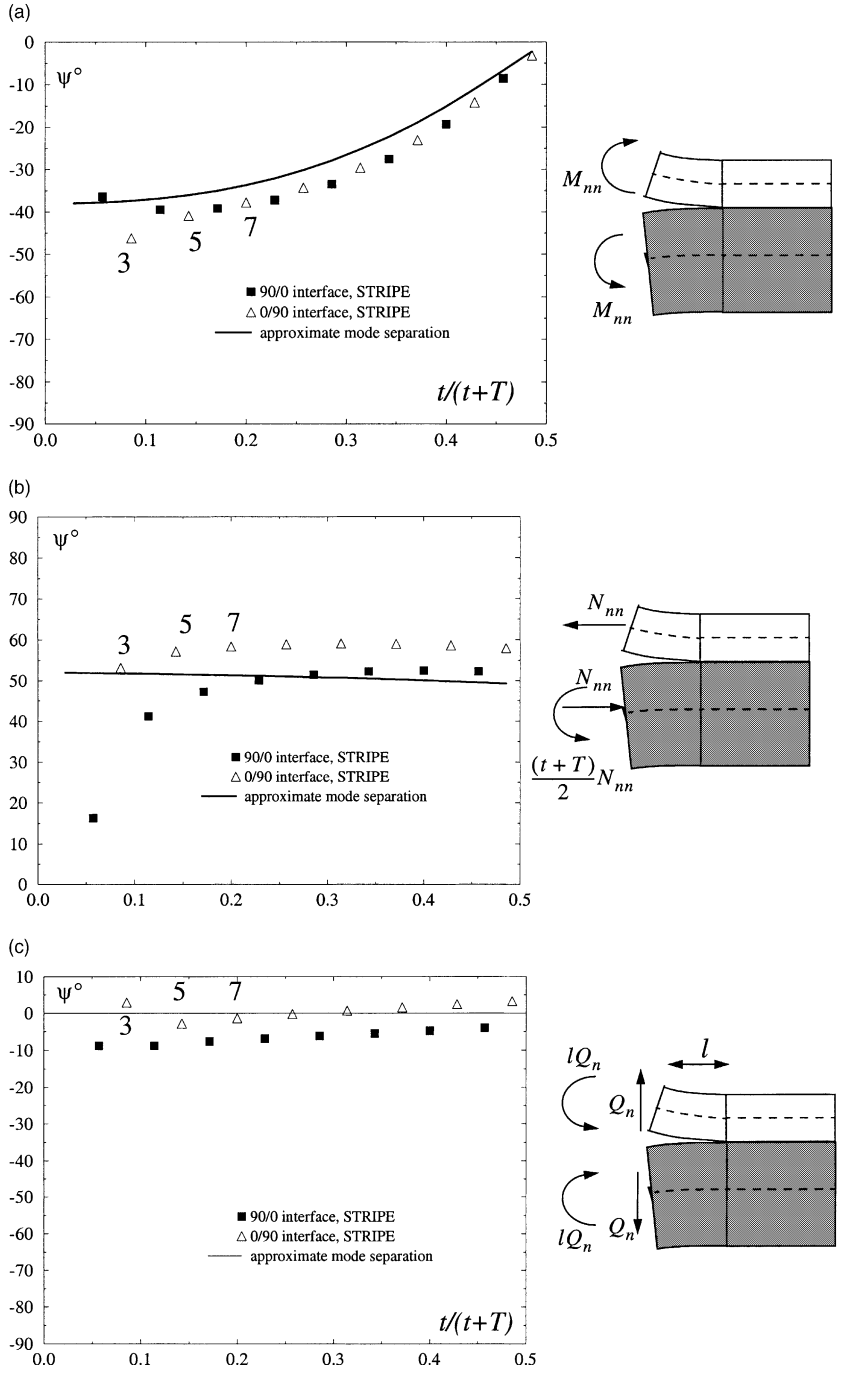

Fig. 14. Computed phase angle, ψ, as function of normalized delamination depth, $t/(t+T)$ for a 0/90-layup with 35 plies as given by *hp*-FE analysis, STRIPE and approximate mode separation (a) $M=1$, $N=0$, $Q=0$, (b) $M=0$, $N=1$, $Q=0$ and (c) $M=0$, $N=0$, $Q=1$.

5.3. Comparison of calculated results and test data

5.3.1. Global buckling load

The calculated buckling load with $L = 150$ mm is 119 kN, which is slightly higher than the experimentally observed buckling load ($\sim$114 kN). In order to investigate if this was due to the particular computational model, the global buckling analysis was also performed in a full three-dimensional FE analysis using the in-house *hp* FE code, STRIPE, where each ply was modelled explicitly. The difference in computed buckling load between the plate model and the refined three-dimensional model was negligible. This lead us to the conjecture that the lower buckling value in the tests was mainly due to nonperfect clamping. This discrepancy was also the reason why the second type of clamping was introduced.

It is well known that a perfect clamping is difficult to achieve experimentally and the buckling load seen in the experiments are usually slightly lower. In the analysis by Kardomateas (1989), a strong influence of the boundary conditions on the buckling loads of a strip delaminated plate in compression was reported. In a study on undelaminated plates, Yeh and Tan (1994) reported an observed buckling load for undelaminated $[0°]_8$ plates which was approximately 10% lower than that predicted by FE analysis.

We saw from the tests that the delamination growth was intimately linked with global panel buckling and in order to have quantitatively accurate results in the analyses, the clamping effect needs to be modelled. The buckling load is more or less proportional to the square of the plate thickness over panel length. A slightly increased panel length therefore has a similar effect on the buckling load as an imperfect clamping. At $L = 150$ mm, 1 mm additional panel length results in a reduction in the buckling load with about 1.5 kN. Instead of attempting to model the flexibility of the clamped ends we have adopted an 'apparent length' for the panel in the analyses such that the computed global buckling load coincides with the one found in the tests. In the analyses, $L = 154$ mm was therefore used. This is of course an unsatisfactorily approach since it requires a priori knowledge of the global buckling load. The alternative to retain the panel length but prescribe a certain flexibility at the clamped edge that gives the observed buckling load, would also require adjustments to test results.

5.3.2. Comparison – thin film versus global bending model

To assess the applicability of the thin film assumption, delamination buckling analyses were performed for the circular delamination configuration for all three delamination depths using the global bending model and the thin film model respectively. Fig. 15a and b shows the resulting out-of-plane deflection in the centre of the upper and lower part and the maximum energy release rate as function of the load for the three-layer delaminated panel. The differences in displacements and energy release rates between the global and thin film models are very small up to half the global buckling load. As the global buckling load is approached the displacements deviate substantially and the energy release rate increases drastically for the global bending model. This is in line with the tests where delamination growth occurred at or slightly below the global buckling load. Note that the load required for energy release rates in the range 250–1000 J/m^2 is substantially higher in the thin film case. Thus the thin film model will not be applicable for analysis of these tests. For the five- and seven-layer delaminations the difference between the global bending and thin film models was even larger.

5.3.3. Modelling of the dial gauge effect

A point force, P_D, of 1 N was applied at the centre of the delaminated member to simulate the dial gauge effect. In accordance with test results, this point force had virtually no effect on the delamination buckling or post-buckling deflection for the five- and seven-layer delaminations. The three-layer delamination buckled at a compressive load of 11.5 kN when there was no point force. When the point force was applied, a bifurcation was found at this load, but the delaminated members remained in contact locally at the point force up to a load of 22.6 kN. The contact force versus the applied load is plotted in Fig. 16. At the load

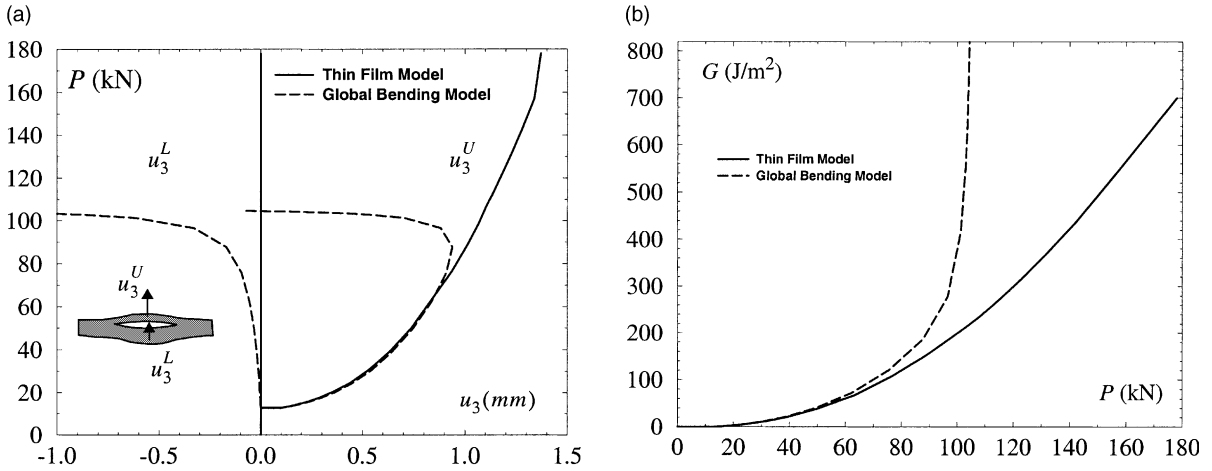

Fig. 15. Comparison between analysis with thin-film assumption and global bending for the three-layer delamination: (a) computed out-of-plane displacement at the centre of delamination for delaminated member and substrate as function of applied load and (b) computed maximum energy release rate, G, as function of applied load, P.

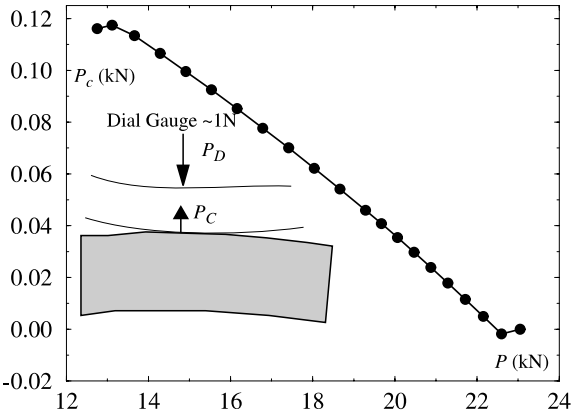

Fig. 16. Computed contact force, P_c, as function of applied compressive load, P.

when the contact force vanishes we expect the delaminated member to snap to a buckled configuration, but we did not succeed to capture this new state in the analyses. In an attempt to capture the out-of-plane deflection with the point force, the buckled configuration with no point force was unloaded with the point force applied. The resulting deflections are shown in Fig. 17. We see that the point force effect is small for loads above 25 kN, but note that the buckled shape collapses at 16 kN when unloaded. The computational results for the three-layer delamination may be summarized as follows: the point force will suppress the delamination buckling; up to 16 kN the delamination will remain closed irrespective if we load or unload; for loads above 22 kN, the delamination will be buckled and the point load has a minor effect; for applied loads between these values, the analysis indicates that there may exist two solutions; a buckled and a closed one.

The out-of-plane deflections for some tested panels with three-layer delamination is also shown in Fig. 17. The panel with thinner double inserts and a dial gauge, A3_4, follows the calculated deflection curve

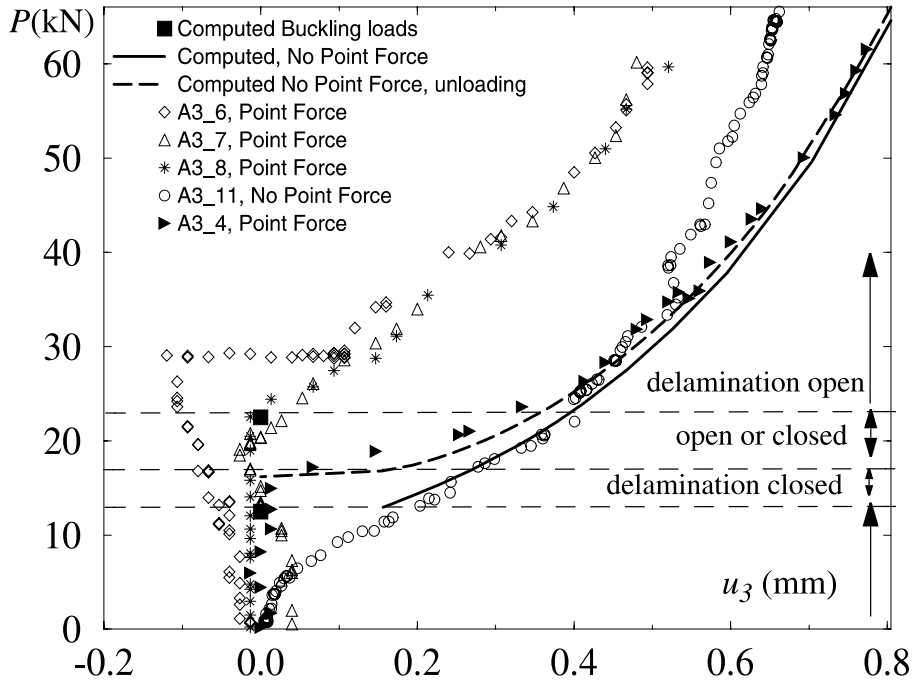

Fig. 17. Computed and measured out-of-plane deflections for delaminated member as a function of applied load, P, for cases with and without point force.

with the point force very well. Four panels with Teflon inserts are also shown with the dial gauge applied on three (A3_6, A3_7 and A3_8) and one with no dial gauge (A3_11). We see clearly that the out-of-plane deflection is delayed for the panels with the dial gauge. The out-of-plane deflection differ for three panels with dial gauges at loads close to the buckling loads, which is in line with the nonuniqueness seen in the analysis. We also see that panels with Teflon inserts have a typical initial imperfection behaviour. Analyses were also performed with an initial imperfection for the delaminated member representing the Teflon insert (25 μm, corresponding to 7% of the delamination thickness), but the effect of this imperfection was very small. As discussed above, we believe that the large panel from which the delaminated panels were cut had some initial curvature. Unfortunately, all panels had been loaded to failure before this conjecture. The assumed curvature of the delaminated panel could therefore not be confirmed. No analyses with an overall panel curvature were run.

5.3.4. Post-buckling of initially circular delamination

Calculated delamination buckling loads with no point force were 11.5, 37.4 and 70.3 kN for the three depths. The maximum load were 108, 108 and 111 kN for the three depths, respectively. These results are in good agreement with the experimental observations. Fig. 18a–c shows the computed central deflection in the upper and lower part as function of the applied load for all three depths along with corresponding deflections from tests for panels (A3_4_2, A3_11_2), (A5_1_1, A5_4_2) and (A7_1_2, A7_5_2). For all panels, the delaminated layer buckles and then initially deflects from the thicker lower layer until it reaches a maximum deflection at a load which more or less coincides with onset of downward deflection of the lower member. From then on, both layers deflect downwards with an increasing opening of the delamination. There is a very good overall correspondence between computations and experiments, but computed results

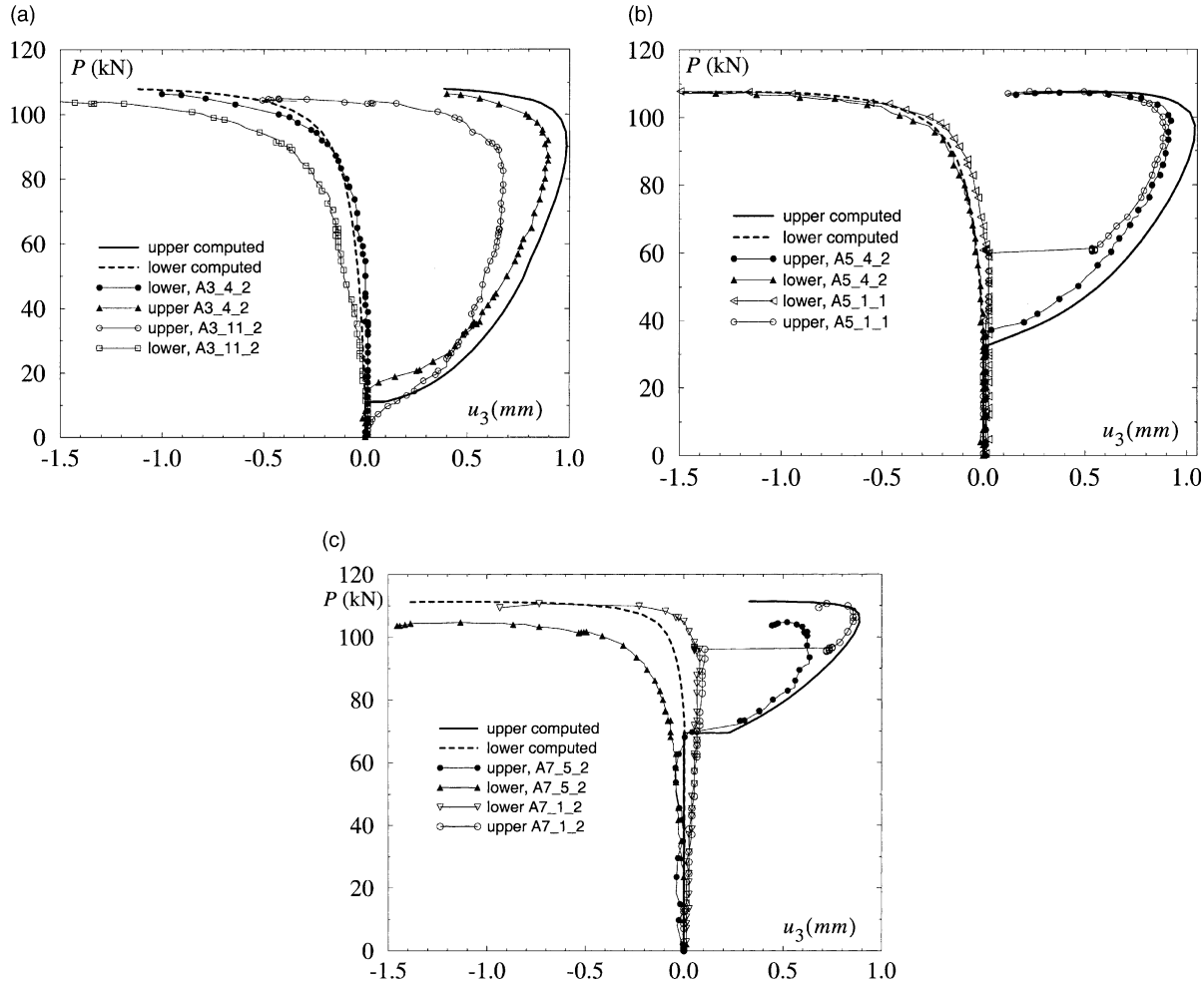

Fig. 18. Computed and measured out-of-plane displacement at the centre of circular delamination as a function of applied load: (a) three-layer delamination, (b) five-layer delamination and (c) seven-layer delamination.

have a tendency to slightly overestimate the maximum deflection of the thin member. The panel, A3_11_2 shows a distinct imperfection behaviour, but it is interesting to note that the opening of the delamination, measured by the difference between upper and lower deflection, is almost the same as in the analysis. For the seven-layer delamination panel, the computed delamination buckling load agrees very well with the test results from the second test series, but predicts a higher maximum load.

The energy release rate as function of the load attained its maximum value perpendicular to the loading direction, (at $s = 1$ in Fig. 4) in all cases. The maximum energy release rates as function of the applied load for the three depths are shown in Fig. 19. The critical energy release rate in pure modes I and II are indicated with dotted lines. The energy release rate increases drastically at the global buckling load and this feature becomes more pronounced with increasing delamination depth.

As seen from the mixed mode fracture tests (Fig. 6), the critical energy release rate is strongly fracture mode dependent, and reliable mode separation of the energy release is therefore in most cases indispensable for accurate prediction of delamination growth. However, in this case, due to the drastic increase in energy

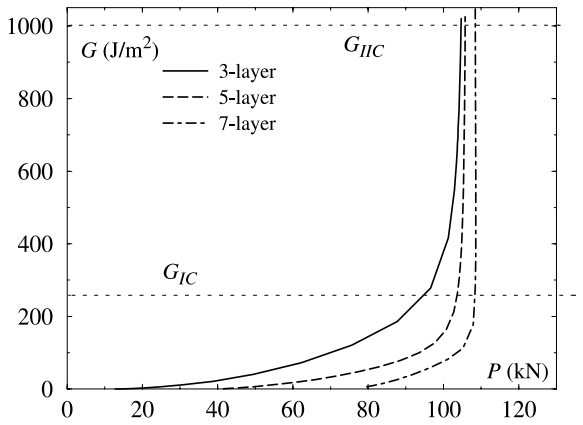

Fig. 19. Computed maximum energy release rate as function of applied load for three-, five- and seven-layer delamination, respectively.

release rate, the load for onset of delamination growth can be predicted fairly well without mode separation.

The load at which crack growth was initiated in the tests was in the second test series in average 105 kN. This is qualitatively in good agreement with the computed energy release rate. We see from Fig. 19 that in the analysis, the energy release for a given load decreases with delamination depth. The fact that load at onset of delamination growth did not increase with delamination depth could imply a higher mode II at delamination growth for the thinner delaminations. It has been found in other studies that in the thin-film case the crack tip loading is primarily mode I at delamination buckling, (Nilsson and Storåkers, 1992; Whitcomb, 1989), but that the mode II loading increases when the applied load normalized with the delamination buckling load increases, which would be in agreement with our tests. The isotropic mode separation given by Eqs. (10)–(12) and (15)–(17), was therefore done for all three delamination depth to see if the same trend could be seen in this case. The resulting phase angle, ψ was, however, close to 50°, i.e. equal mode I and mode II, for all delaminations depths at 105 kN applied load. This value is consistent with the shear cusps and ribs seen in the fractographical investigation.

Contact was encountered in the analysis for all three depths already at buckling and were larger the thinner the delamination. The contact area then expanded as the load increased. The contact areas at onset of delamination growth for the three-layer delamination and at delamination buckling for the seven-layer delamination are depicted in Fig. 20.

5.3.5. Analysis of delamination growth

Delamination propagation for the three delamination depths was simulated following the crack growth procedure outlined earlier. Two different fracture toughnesses were adopted. The first one used a mode independent fracture toughness with 450 J/m^2. The value $G_c = 450$ J/m^2 fits the load for onset of delamination growth, 105 kN, and corresponds to a critical G at 50% mode II for this material (Fig. 6). The second one adopted the mixed mode dependent fracture toughness defined by Eq. (20) with $G_{IC} = 250$ J/m^2, $a_1 = -0.10$, $\lambda = 0.22$, depicted in Fig. 6.

Fig. 21 shows the corresponding fronts for the three depths at 7.5 and 15 mm growth perpendicular to the loading for $G_c = 450$ J/m^2. This trend was also observed in the experiments as seen in Fig. 12. The corresponding fronts for the mode dependent criterion were very similar but slightly narrower. The mesh of the delaminated region at 15 mm growth with associated contact zone is shown in Fig. 22 for the three-layer delamination. The mesh becomes gradually distorted as the delamination progresses. For simulation of

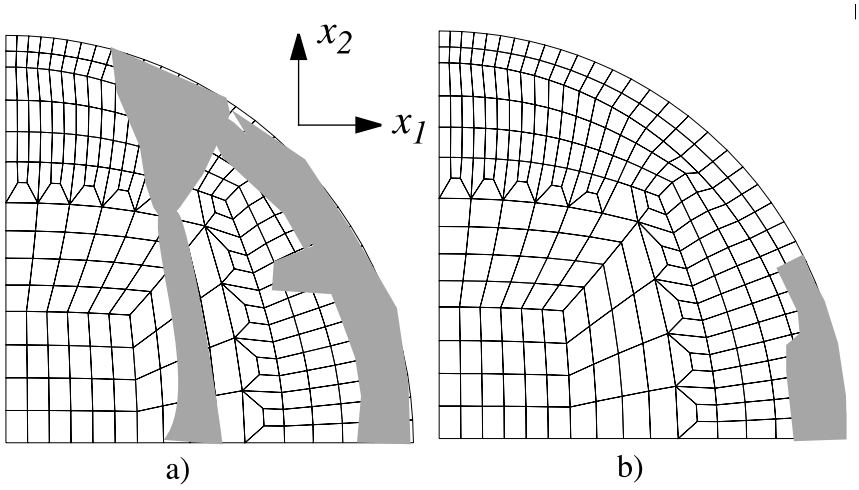

Fig. 20. Sketch of computed contact areas: (a) three-layer delamination at onset of delamination growth and (b) seven-layer delamination at delamination buckling.

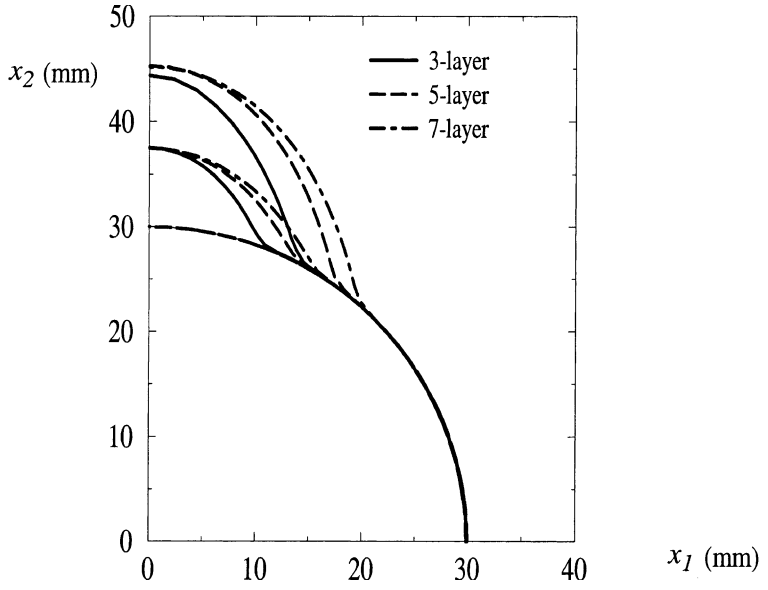

Fig. 21. Computed shape of the delamination front at 7.5 and 15 mm growth for the three-, five- and seven-layer delaminations respectively. Crack growth criterion: $G = G_c = 450$ J/m^2.

extensive growth, say double compared to this analysis, a total remeshing would be needed with additional elements in the growth region.

The distributions of the normalized energy release rate along the delamination fronts in Fig. 21 are depicted in Fig. 23 when $G_c = 450$ J/m^2. We see that the gradient in energy release rate is more pronounced for the thinner delamination. The plateau seen in the G-distribution, which increases with delamination

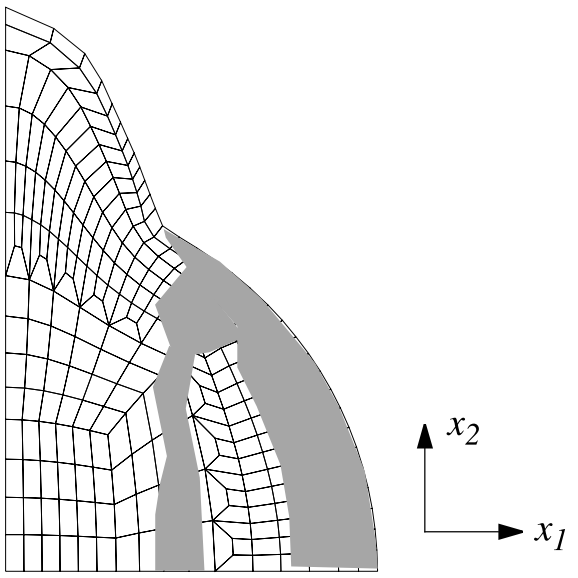

Fig. 22. FE mesh at 15 mm growth and associated contact area for the three-layer delamination.

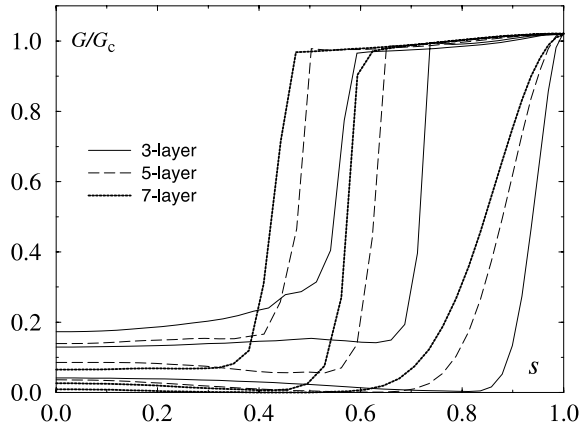

Fig. 23. The energy release rate distribution at initial growth, 25% growth and 50% growth for the three-, five- and seven-layer delaminations, respectively. Crack growth criterion is $G = G_c = 450$ J/m^2.

growth, is a measure of the length of the front that propagates. The absence of spurious variation of the energy release rate along the propagating part of the front indicates that the adopted crack growth increment is sufficiently small. The normalized G-distributions with the mode dependent fracture toughnesses are very similar.

The applied displacement, u_0, for continuous crack growth and the associated reaction load, P, as function of the growth in the transverse direction for the two fracture toughness criteria are shown in Fig. 24a and b respectively. The calculated applied displacement for continuous growth for all three depths and fracture criteria increases monotonically whereas in the experiments delamination growth was initially semi-stable for all depths followed by a shift to unstable growth for the five- and seven-layer delaminations.

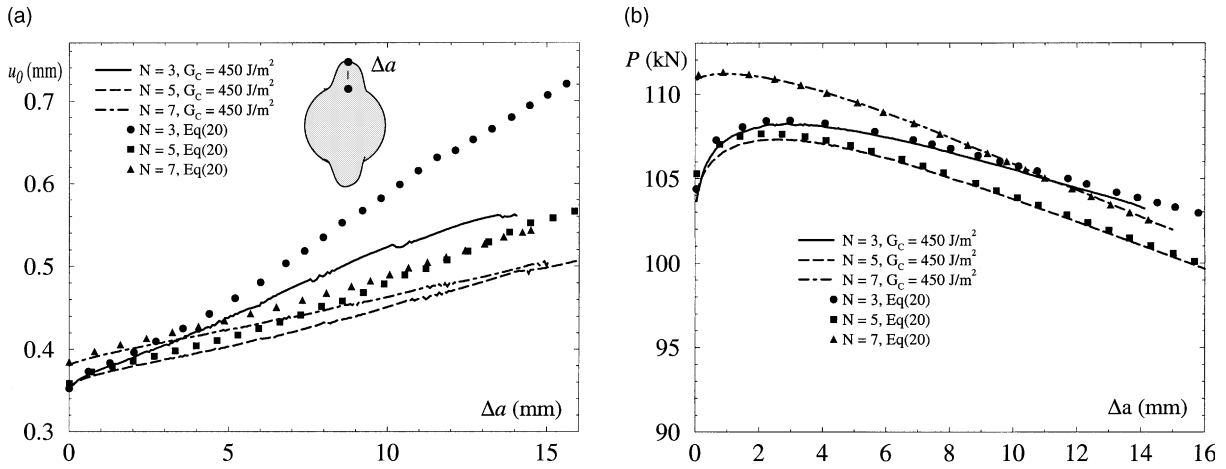

Fig. 24. Computed applied displacement and reaction load as function of growth, Δa, for the three-, five- and seven-layer delaminations, respectively for the two crack growth criteria: (a) displacement load and (b) reaction load.

The simulations predict stable growth for all cases, but the increase in load is much larger for the three-layer delamination. The mode dependent fracture toughness gives a considerably more stable growth for the three-layer delamination and a slightly more stable growth for the two other depths. The reaction load on the other hand is virtually unaffected by the fracture criterion. The phase angle as a function of growth when the mode dependent fracture criterion is used is plotted in Fig. 25 for the three depths. The mode II loading increases with delamination growth and this is most pronounced for the three-layer delamination. The stability properties depend on the changing mode mixity during growth as well as the shape of the delamination. A more localized delamination growth gives a larger gradient in the G-distribution as we saw in Fig. 23, which has a stabilizing effect.

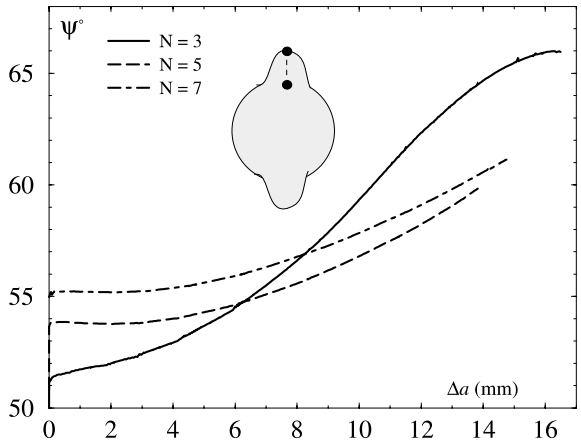

Fig. 25. Computed phase angle, ψ, as function of growth, Δa, at the point perpendicular to the load (see inset) for the mixed mode crack growth criterion.

6. Conclusions

The tests as well as the numerical analyses for all delamination depths showed a very strong interaction between delamination growth and global buckling load. The dimensions for delamination and panel in this study were representative for a wing skin and the interaction seen here is therefore not unrealistic. Quasi-isotropic layups are more common than cross-plies in aircraft applications. However, the main observations are not affected by this. One important conclusion, at least for the geometries and materials studied here, is that the so-called thin film assumption is not adequate to predict growth, not even for the three-layer delamination where the thickness was less than one tenth of the plate thickness. Thus, a delamination buckling analysis should always be accompanied by a global buckling analysis. If delamination growth occurs at loads significantly lower that the global buckling load, say two thirds, then the thin film model may be adopted. At the global buckling load, crack growth parameters increase drastically with the applied load and growth will be predicted fairly accurately irrespective of the sophistication of the fracture model. On the basis of these findings, aircraft structures that may contain delaminations should not be allowed to buckle globally.

The computational model was very successful in predicting delamination buckling load including the intricate effect of the dial gauge. Successful predictions of the delamination buckling problem for slender structures require that the global buckling load is accurately determined. In this study, the length of the panel was adjusted slightly to accommodate the nonperfect clamping conditions. With this ad hoc modelling, out-of-plane deflections, shape of delamination front after growth as well as the load for onset of delamination growth were accurately predicted. In the analyses, two different crack growth criteria were adopted, one with a constant G_c and one with fracture mode dependence. In all cases, the analysis predict that the load for onset of delamination growth should increase slightly but consistently with delamination depth. The analyses also predict stable delamination growth for all delamination depths. In the tests, onset of delamination growth occurred almost at the same load and delamination growth was initially semi-stable with a shift to unstable growth for the five- and seven-layer delaminations. This discrepancy could be related to the strongly mode dependent fracture toughness in combination with more mode I loading in the tests than predicted by the isotropic mode separation. It could also be due to a slightly different coupling between the global plate deflection and the delaminated member in the tests than predicted.

The third objective of the investigation was the development of reliable test procedures. Proper separation between the delaminated members is essential to achieve repeatability and consistency of experiments and Teflon insert proved to be superior to the polyimide inserts. For the thinner delaminations, the small force exerted by the dial gauge could be sufficient to influence the post-buckling behaviour of the most shallow delaminations. Therefore, out-of-plane displacement of the delaminated member should be measured by a noncontact tool, e.g. by a laser instrument. Due to the strong interaction between delamination growth and global buckling, it is important that uncertainties in boundary conditions, which strongly affects the global buckling load, are minimized.

The work presented in this paper constitute the first steps towards a robust and reliable methodology for assessing damage in aircraft structures. Our strategy is to develop the computational models in combination with discriminate testing, where tests are used to assess the computational model; as a tool to indicate priorities in the model development; and provide reliable material data.

The next step in the modelling, which is presently in progress, will be to implement the reliable and complete mode decomposition outlined here. This is a straight-forward procedure where the mixed-mode coefficients in Eq. (10) are determined for the particular material combination and delamination depth using stress intensities defined by Eq. (14). These coefficients can be saved in a database from which coefficients are taken during analysis. The interpretation and application of different alternatives to describe the mode mixity is still an open issue that needs to be addressed in future research. It is worth mentioning in this context that delaminations tend to propagate in certain interfaces with growth parallel to fibres

(e.g. Greenhalgh et al., 1999). This implies that the apparent fracture toughness is not only a function of mode mixity, but also on the fibre orientation of adjacent plies. This requires basic fracture tests with different fibre orientations.

The single delamination model is relevant for manufacturing defects. Multiple delaminations of equal size may lower the failure load significantly (e.g. Kyoung et al., 1999). Recent tests reported in Asp et al. (1999) show, however, that panels with natural impact damage failed primarily by delamination growth where one delamination turned out to be dominant. The reason for this is that after impact, delaminations differ in size and the largest ones are often found relatively close to the surface and only very few actually buckle. This suggests that modelling of multiple and interacting buckled delaminations is not as urgent as anticipated. Instead, effort should be given to model the reduced stiffness due to matrix cracking, broken fibres and unbuckled delaminations.

References

Abrate, S., 1991. Impact on laminated composite materials. Appl. Mech. Rev. 44, 155–190.

Abrate, S., 1994. Impact on laminated composites: recent advances. Appl. Mech. Rev. 47, 517–544.

Andersson, B., Babuska, I., Falk, U., 1990. Accurate and reliable determination of edge and vertex stress intensity factors in three-dimensional elastomechanics. In: ICAS-90-4.9.2, Proceedings of 17th congress of the International Council of the Aeronautical Sciences. Stockholm, Sweden, pp. 1730–1746.

Andersson, B., 1993. Calculation of Fracture mechanics parameters from measured surface displacements in composite specimens. In: Proceedings from Sixth Nordic Seminar on Computational Mechanics. October 18–19, University of Linköping, pp. 181–184.

Asp, L.E., Nilsson, S., Singh, S., 1999. An experimental investigation of the influence of delamination growth on the residual strength of impacted laminates, FFA TN 1998-52. The Aeronautical Research Institute of Sweden (Proceedings of Euromech Colloqium 400, London, UK, September 1999) 158–165.

Chai, H., Babcock, C.D., Knauss, W.G., 1981. One-dimensional modeling of failure in laminated plates by delamination buckling. Int. J. Solids Struct. 17, 1069–1083.

Chai, H., Babcock, C.D., 1985. Two-dimensional modelling of compressive failure in delaminated plates. J. Compos. Mater. 19, 67–98.

Giannakopolous, A., Nilsson, K.-F., Tsamasphyros, G., 1995. The contact problem at delamination. J. Appl. Mech. 62, 989–996.

Greenhalgh, E., Singh, S., K.-F. Nilsson, 1999. Mechanisms and Modelling of Delamination Growth and Failure of Carbon-Fibre Reinforced Skin-Stringer Panels, ASTM D-30, Composite Structures: Theory and Practice. Seattle, Washington, USA (to be published in ASTM STP 1383).

Hutchinson, J.W., Suo, Z., 1992. Mixed mode cracking in layered materials. Advances in Applied Mechanics, vol. 28. Academic Press, New York, pp. 63–191.

Juntti, M., Asp, L.E., Olsson, R., 1999. Assessment of evaluation methods for the mixed-mode bending test. J. Compos. Technol. Res. 21, 37–48.

Kardomateas, G.A., 1989. End fixity effects on the post-buckling of delaminated composites. Compos. Sci. Technol. 34, 113–128.

Kim, H.-J., 1996. Effect of delamination on buckling behavior of quasi-isotropic laminates. J. Reinf. Plast. Compos. 15, 1262–1277.

Kyoung, W.-M., Kim, C.-G., Hong, C.-S., 1999. Buckling and postbuckling of composite cross-ply laminates with multiple delaminations. Compos. Struct. 43, 257–274.

Lekhnitskii, S.G., 1963. Theory of Elasticity of an anisotropic body. Holden-Day, San Francisco, USA.

Nilsson, K.-F., Storåkers, B., 1992. On the interface crack growth in composite plates. J. Appl. Mech. 59, 530–538.

Nilsson, K.-F., 1993. On growth of crack fronts in the DCB-test. Comp. Engng. 3, 527–546.

Nilsson, K.-F., Thesken, J.C., Sindelar, P., Giannakopoulos, A., Storåkers, B., 1993. A theoretical and experimental investigation of buckling induced delamination growth. J. Mech. Phys. Solids 41, 749–782.

Nilsson, K.-F., Giannakopoulos, A., 1995. A finite element analysis of configurational stability and finite growth of buckling-driven delamination. J. Mech. Phys. Solids 43, 1983–2021.

Nilsson, K.-F., Asp, L.E., Alpman, J.E., 1997. Delamination buckling and growth at global buckling. In: Rossmanith, H.-P. (Ed.), First International Conference on Damage and Fracture of Interfaces, DFI-1. Vienna, September 1997, pp. 193–202.

Nilsson, K.-F., Asp, L.E., Sjögren, A., 2000. On transition of delamination growth behaviour for compression loaded composite panels, FFA-TN 2000-19. Aeronautical Research Institute of Sweden.

Olsson, R., Thesken, J.C., Brandt, F., Jönsson, N., Nilsson, S., 1996. Investigations of delamination criticality and the transferability of growth criteria. Compos. Struct. 36, 221–247.

Pavier, M.J., Clarke, M.P., 1996. Finite element prediction of the post-impact compressive strength of fibre composites. Compos. Struct. 36, 141–153.

Rice, J.R., 1988. Elastic fracture mechanics concepts for interfacial cracks. J. Appl. Mech. 55, 98–103.

Sheinman, I., Kardomateas, G.A., 1997. Energy release rate and stress intensity factors for delaminated composite laminates. Int. J. Solids Struct. 34, 451–459.

Sheinman, I., Kardomateas, G.A., Pelegri, A.A., 1998. Delamination growth during pre- and post-buckling phases of delaminated composite laminates. Int. J. Solids Struct. 35, 19–31.

Simitses, G.J., Sallam, S., Yin, W.L., 1985. Effect of delamination of axially loaded homogeneous laminated plates. AIAA J. 23, 1437–1444.

Storåkers, B., Andersson, B., 1988. Nonlinear plate theory applied to delamination in composites. J. Mech. Phys. Solids 36, 689–718.

Suo, Z., Hutchinson, J.W., 1990. Interface crack between two elastic layers. Int. J. Fract. 43, 1–18.

Wang, S.S., Choi, I., 1982. Boundary-layer effects in composite laminates: Part 1. Freeedge stress singularities, Part 2. Free edge stress solutions and basic characteristics. J. Appl. Mech. 49, 541–560.

Whitcomb, J.D., 1981. Finite element analysis of instability related delamination growth. J. Compos. Mater. 15, 403–426.

Whitcomb, J.D., 1986. Parametric analytical study of instability-related delamination growth. Compos. Sci. Technol. 25, 19–48.

Whitcomb, J.D., 1989. Three-dimensional analysis of a post-buckled embedded delamination. J. Compos. Mater. 23, 862–889.

Whitcomb, J.D., 1992. Analysis of a laminate with a postbuckled embedded delamination including contact effects. J. Compos. Mater. 26, 1523–1535.

Yeh, M.-K., Tan, C.-M., 1994. Buckling of elliptically delaminated composite plates. J. Compos. Mater. 28, 36–52.